Nonperturbative determination of the Collins-Soper kernel from quasitransverse-momentum-dependent wave functions

Min-Huan Chu,[1,2] Zhi-Fu Deng,[2] Jun Hua,[3,4,2] Xiangdong Ji,[5,6] Andreas Schäfer,[7] Yushan Su,[5] Peng Sun,[8] Wei Wang,[2,*] Yi-Bo Yang,[9,10,11,12] Jun Zeng,[2] Jialu Zhang,[2] Jian-Hui Zhang,[13] and Qi-An Zhang[14,15,†]

[1]*Yang Yuanqing Scientific Computing Center, Tsung-Dao Lee Institute, Shanghai Jiao Tong University, Shanghai 200240, China*
[2]*INPAC, Key Laboratory for Particle Astrophysics and Cosmology (MOE), Shanghai Key Laboratory for Particle Physics and Cosmology, School of Physics and Astronomy, Shanghai Jiao Tong University, Shanghai 200240, China*
[3]*Guangdong Provincial Key Laboratory of Nuclear Science, Institute of Quantum Matter, South China Normal University, Guangzhou 510006, China*
[4]*Guangdong-Hong Kong Joint Laboratory of Quantum Matter, Southern Nuclear Science Computing Center, South China Normal University, Guangzhou 510006, China*
[5]*Department of Physics, University of Maryland, College Park, Maryland 20742, USA*
[6]*Center for Nuclear Femtography, 1201 New York Avenue NW, Washington, D.C. 20005, USA*
[7]*Institut für Theoretische Physik, Universität Regensburg, D-93040 Regensburg, Germany*
[8]*Nanjing Normal University, Nanjing, Jiangsu 210023, China*
[9]*CAS Key Laboratory of Theoretical Physics, Institute of Theoretical Physics, Chinese Academy of Sciences, Beijing 100190, China*
[10]*School of Fundamental Physics and Mathematical Sciences, Hangzhou Institute for Advanced Study, UCAS, Hangzhou 310024, China*
[11]*International Centre for Theoretical Physics Asia-Pacific, Beijing/Hangzhou, China*
[12]*School of Physical Sciences, University of Chinese Academy of Sciences, Beijing 100049, China*
[13]*Department of Physics, Center of Advanced Quantum Studies, Beijing Normal University, Beijing 100875, China*
[14]*School of Physics, Beihang University, Beijing 102206, China*
[15]*Key Laboratory for Particle Astrophysics and Cosmology (MOE), Shanghai Key Laboratory for Particle Physics and Cosmology, Tsung-Dao Lee Institute, Shanghai Jiao Tong University, Shanghai 200240, China*

(Received 9 April 2022; accepted 27 July 2022; published 22 August 2022)

In the framework of large-momentum effective theory at one-loop matching accuracy, we perform a lattice calculation of the Collins-Soper kernel, which governs the rapidity evolution of transverse-momentum-dependent (TMD) distributions. We first obtain the quasi-TMD wave functions at three different meson momenta, on a lattice with valence clover quarks on a dynamical highly improved staggered quark sea and lattice spacing $a = 0.12$ fm from the MILC Collaboration, and renormalize the pertinent linear divergences using Wilson loops. Through one-loop matching to the light-cone wave functions, we determine the Collins-Soper kernel with transverse separation up to 0.6 fm. We study the systematic uncertainties from operator mixing and scale dependence, as well as the impact from higher power corrections. Our results potentially allow for a determination of the soft function and other transverse-momentum-dependent quantities at one-loop accuracy.

DOI: 10.1103/PhysRevD.106.034509

[*]Corresponding author.
wei.wang@sjtu.edu.cn
[†]Corresponding author.
zhangqa@buaa.edu.cn

I. INTRODUCTION

Understanding the internal three-dimensional structure of hadrons, such as the proton, is an important goal in nuclear and particle physics. In this regard, the transverse momentum-dependent (TMD) parton distribution functions (TMDPDFs) [1,2] play an important role, as they characterize their intrinsic transverse partonic structure. These distributions are also essential ingredients in the description

of multiscale and noninclusive processes, such as Drell-Yan production of electroweak gauge bosons, Higgs bosons, or semi-inclusive deep-inelastic scattering with small transverse momentum, in the context of QCD factorization theorems. As a result, they have received considerable attention in the past few decades (for a review, see Ref. [3]). More accurate experimental measurements are expected in the coming decades from Jefferson Laboratory 12 GeV [4] and the electron-ion colliders in the U.S. [5,6] and China [7].

In contrast to the TMDPDFs that encode the probability density of parton momenta in hadrons, the transverse momentum-dependent wave functions (TMDWFs) offer a probability amplitude description of the partonic structure of hadrons, from which one can potentially calculate various quark/gluon distributions. In the QCD factorization involving transverse momentum, they are the most important ingredients to predict physical observables in exclusive processes, for instance, weak decays of heavy B mesons [8,9], which are valuable to extract the Cabibbo-Kobayashi-Maskawa matrix element and to probe new physics beyond the standard model. However, due to the lack of knowledge of TMDWFs, the one-dimensional light-cone distribution amplitudes (LCDAs) are used instead in most analyses of B decays [8–10], resulting in uncontrollable errors. The unprecedented precision of experimental measurements of B decays [11] urgently requires a reliable theoretical knowledge of TMDWFs.

A common feature of TMDPDFs and TMDWFs is that they depend both on the longitudinal momentum fraction x and on the transverse spatial separation of partons. Considerable theoretical efforts have been devoted in recent years to determine these quantities by fitting the pertinent experimental data [12–20], which, however, is limited by the imprecise knowledge of the nonperturbative behavior of TMDPDFs and TMDWFs. Thus, it is highly desirable to develop a method to calculate them from first-principle approaches such as lattice QCD.

This has been realized in the framework of large-momentum effective theory [21,22], which offers a systematic way to calculate light-cone correlations by simulating time-independent Euclidean correlations on the lattice. Significant progress has been made in calculating various parton quantities from large-momentum effective field theory (LaMET). For recent reviews, see Refs. [23,24].

A very important result of LaMET development is that the TMDPDFs and TMDWFs can be calculated through the Euclidean quasi-TMDPDFs and quasi-TMDWFs, as well as a universal soft function (factor) [25–29]. In Ref. [26], it has been suggested that the form factor of a bilocal four-quark operator calculable on the lattice can be factorized into quasi-TMDWFs, a universal soft (function) factor, and the matching kernel through QCD factorization at large-momentum transfer, allowing for the first time calculation of the universal soft function on the lattice. Thus, the light-cone TMD parton distributions and wave functions can be obtained from numerical calculations of the four-quark form factors and quasi-TMDPDFs and TMDWFs on the lattice [26,27]. On the other hand, one can also make use of the QCD factorization to obtain the Collins-Soper (CS) kernel from quasi-TMDPDFs and TMDWFs. The first results for the CS kernel based on these proposals have been published recently [30–35]. The quasi-TMDWFs approach to the CS kernel requires two-point function calculations and potentially can reach the light-cone limit with relatively small hadron momenta.

In this work, we present a state-of-the-art calculation of the CS kernel, based on a lattice QCD analysis of quasi-TMDWFs with $N_f = 2 + 1 + 1$ valence clover fermions on a staggered quark sea with one-loop matching accuracy. A single ensemble with lattice spacing $a \simeq 0.12$ fm, volume $n_s^3 \times n_t = 48^3 \times 64$, and physical sea-quark masses is used. In order to improve the signal-to-noise ratio, we tune the light-valence quark masses such that $m_\pi = 670$ MeV. The CS kernel is then extracted through the ratios of the quasi-TMDWFs and the perturbative matching kernels at different momenta, $P^z = 2\pi/n_s \times \{8, 10, 12\} = \{1.72, 2.15, 2.58\}$ GeV. This corresponds to Lorentz boost factors $\gamma = \{2.57, 3.21, 3.85\}$, respectively. This analysis improves the previous ones [31,33] by taking into account the one-loop perturbative contributions and by analyzing systematic uncertainties from operator mixing, higher-order corrections from the scale dependence, and higher power corrections in terms of $1/P^z$.

The remainder of this paper is organized as follows. In Sec. II, we present the theoretical framework to extract the CS kernel from quasi-TMDWFs. Numerical results for quasi-TMDWFs and the CS kernel are presented in Sec. III. A brief summary of this work is given in Sec. IV. More details about the analysis are collected in the Appendixes.

II. THEORETICAL FRAMEWORK

In this section, we review the necessary theoretical background for the present calculation. We present the definitions of the CS kernel and rapidity evolution and introduce the quasi-TMD wave functions. We then discuss the factorization of the quasi-TMDWFs and its connection with the CS kernel.

A. Collins-Soper kernel and rapidity evolution

Unlike the collinear light-cone PDFs and distribution amplitudes, the TMDPDFs and TMDWFs depend on both the renormalization scale μ and an additional rapidity renormalization scale. The latter arises because the matrix elements also suffer from so-called rapidity divergences that require a dedicated regulator [1,36,37]. In TMD factorizations, the contributions of hard, i.e., highly off-shell, modes to the tree process are usually calculated in the dimensional regularization scheme. Collinear modes, which are related

to highly boosted partons in distinct directions, and soft modes, whose typical momentum are at the order $\Lambda_{\rm QCD}$, share the same virtuality and are only distinguishable by their rapidity. In calculations using regularization schemes such as dimensional regularization, which only regulate ultraviolet divergences, one will encounter additional rapidity divergences that arise in soft and collinear matrix elements when integrating over rapidity and have to be resolved using a dedicated regulator. After the later regularization, TMDPDFs and TMDWFs acquire an additional rapidity scale dependence. This dependence should cancel in theoretical predictions for physical observables.

The CS kernel $K(b_\perp,\mu)$, known as the rapidity anomalous dimension, encodes the rapidity dependence of the TMD distributions [1,2],

$$2\zeta\frac{d}{d\zeta}\ln f^{\rm TMD}(x,b_\perp,\mu,\zeta)=K(b_\perp,\mu), \tag{1}$$

where $f^{\rm TMD}$ denotes any leading twist TMDPDF or TMDWF. The TMD distributions depend on the longitudinal momentum fraction x and transverse spatial separation $b_\perp$, which is the Fourier conjugate to the transverse momentum $k_\perp$, as well as the renormalization scale μ and rapidity scale ζ, which is related to the hadron momentum. The μ dependence of the CS kernel $K(b_\perp,\mu)$ satisfies the renormalization group equation (RGE),

$$\mu^2\frac{d}{d\mu^2}K(b_\perp,\mu)=-\Gamma_{\rm cusp}(\alpha_s). \tag{2}$$

Here $\Gamma_{\rm cusp}(\alpha_s)=\alpha_s C_F/\pi+\mathcal{O}(\alpha_s^2)$ is the cusp anomalous dimension, which has been calculated in perturbation theory up to two loops in Ref. [38] and three loops in Ref. [39]. The solution to the RGE can be expressed as

$$K(b_\perp,\mu)=-2\int_{1/b_\perp}^{\mu}\frac{{\rm d}\mu'}{\mu'}\Gamma_{\rm cusp}(\alpha_s(\mu'))+K(\alpha_s(1/b_\perp)). \tag{3}$$

For large $b_\perp$ with $b_\perp^{-1}\lesssim\Lambda_{\rm QCD}$, the CS kernel becomes nonperturbative, which is represented by the noncusp anomalous dimension $K(\alpha_s(1/b_\perp))$ in the above equation.

In the past decades, the CS kernel has been widely studied in global fits of TMD parton distributions [12–20]. The explicit form in the nonperturbative region can only be parametrized by extending the perturbative expressions at small $b_\perp$, which inevitably introduces systematic uncertainties. A direct calculation of TMDPDFs and the relevant CS kernel on the lattice was an almost insurmountable hurdle until the establishment of LaMET [21,22]. A remarkable recent development in LaMET is that these quantities can be accessed through the corresponding quasiobservables [25–28].

B. Quasi-TMD wave functions

As stated above, one can define the quasi-TMDWFs for a highly boosted pseudoscalar meson along the z direction with large momentum P^z as

$$\tilde\Psi^{\pm}(x,b_\perp,\mu,\zeta_z)=\lim_{L\to\infty}\int\frac{dz}{2\pi}e^{ix_r zP^z}\frac{\tilde\Phi^{\pm 0}(z,b_\perp,P^z,a,L)}{\sqrt{Z_E(2L,b_\perp,\mu,a)}}, \tag{4}$$

where $x_r=x-\frac{1}{2}$. The unsubtracted quasi-TMDWF $\tilde\Phi^{\pm 0}$ is defined as an equal-time correlator containing a nonlocal quark bilinear operator with staple-shaped gauge link,

$$\begin{aligned}&\tilde\Phi^{\pm 0}(z,b_\perp,P^z,a,L)\\&=\langle 0|\bar\psi(z\hat n_z/2+b_\perp\hat n_\perp)\Gamma\\&\quad\times U_{\sqsupset,\pm L}(z\hat n_z/2+b_\perp\hat n_\perp,-z\hat n_z/2)\psi(-z\hat n_z/2)|P^z\rangle.\end{aligned} \tag{5}$$

For a pseudoscalar mesonic state, the Dirac structure Γ can be chosen as $\gamma^z\gamma_5$ or $\gamma^t\gamma_5$, which approaches the leading-twist structure $\gamma^+\gamma_5$ in the light-cone limit. With a large but finite P^z, the deviations between $\gamma^z\gamma_5$ and $\gamma^t\gamma_5$ are power suppressed. At one-loop level and leading power accuracy in LaMET, their matching kernels are identical. So technically, one can also use a combination of them, such as $(\gamma^z\gamma_5+\gamma^t\gamma_5)/2$ to minimize power corrections, and the difference between the average and $\gamma^{z/t}\gamma_5$ can be treated as systematic uncertainties arising from higher powers. More details can be found in Sec. III C. Various combinations were also explored in Ref. [33]. The superscript "0" in $\tilde\Phi^{\pm 0}$ indicates bare quantities. The linear divergences come from the self-energy of the gauge link,

$$\begin{aligned}&U_{\sqsupset,\pm L}(z\hat n_z/2+b_\perp\hat n_\perp,-z\hat n_z/2)\\&\quad\equiv U_z^\dagger(z\hat n_z/2+b_\perp\hat n_\perp;L)U_\perp((L-z/2)\hat n_z;b_T)\\&\qquad\times U_z(-z\hat n_z/2;L),\end{aligned} \tag{6}$$

and does not appear as a pole at $d=4$ in dimensional regularization. The Euclidean gauge link in $U_{\sqsupset,\pm L}$ is defined as

$$U_z(\xi,\pm L)=\mathcal{P}\exp\left[-ig\int_{\xi^z}^{\pm L}d\lambda n_z\cdot A(\vec\xi_\perp+n_z\lambda)\right], \tag{7}$$

where $\xi^z=-\xi\cdot n_z$. The $\pm L$ corresponds to the farthest position that the gauge link can reach in the positive or negative n_z direction on a finite Euclidean lattice. This is depicted as the blue and red lines in Fig. 1.

Since the linear divergence is associated with the gauge link, it can be removed by a similar gauge link with the same total length. An optional choice is to make use of the Wilson loop, denoted as Z_E. The Wilson loop can be chosen as the vacuum expectation of a flat rectangular Euclidean Wilson loop in the $z-\perp$ plane,

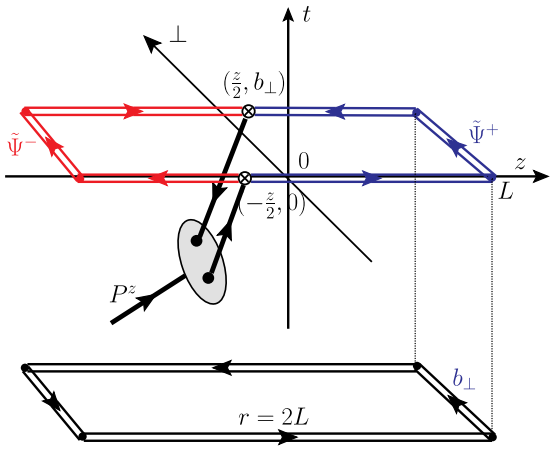

FIG. 1. Illustration of the staple-shaped gauge link included in unsubtracted quasi-TMDWFs and the related Wilson loop. The blue and red double lines in the upper panel represent the L-shift direction on the Euclidean lattice, and the lower panel shows the corresponding Wilson loop, which will subtract UV logarithmic and linear divergences in quasi-TMDWFs.

$$Z_E(2L, b_\perp, \mu, a) = \frac{1}{N_c}\mathrm{Tr}\langle 0|U_\perp(0; b_\perp)U_z(b_\perp \hat{n}_\perp; 2L)|0\rangle. \tag{8}$$

Here the length of Z_E is twice that of the staple-shaped gauge link $U_z^{(\dagger)}$ in the z direction, and thus it is anticipated that the square root of $Z_E(2L, b_\perp, \mu)$ cancels the linear divergence and heavy quark potential in the gauge link. There are residual logarithmic divergences from the vertex of the Wilson line and light quark, which can be renormalized in dimensional regularization [40]. As these logarithmic divergences are independent of z, $b_\perp$, P_z, and L, they will explicitly cancel out when the ratio of quasi-TMDWFs is studied.

C. Factorization of quasi-TMDWFs

With the help of the soft function, the infrared contributions in the subtracted quasi-TMDWFs can be properly accounted for such that the infrared structures for the quasi-TMDWFs and light-cone ones are matched. This implies a multiplicative factorization theorem in the framework of LaMET [25–28,41],

$$\begin{aligned}&\tilde{\Psi}^\pm(x, b_\perp, \mu, \zeta_z)S_r^{1/2}(b_\perp, \mu)\\ &= H^\pm(\zeta_z, \bar{\zeta}_z, \mu^2)\exp\left[\frac{1}{2}K(b_\perp, \mu)\ln\frac{\mp\zeta_z - i\epsilon}{\zeta}\right]\\ &\times \Psi^\pm(x, b_\perp, \mu, \zeta) + \mathcal{O}\left(\frac{\Lambda_{\mathrm{QCD}}^2}{\zeta_z}, M^2\zeta_z, \frac{1}{b_\perp^2\zeta_z}\right),\end{aligned} \tag{9}$$

where the superscript $\pm$ in Eq. (9) corresponds to the direction in the Wilson line, and $\Psi^\pm$ is the TMDWFs defined in the infinite momentum frame. The reduced soft function $S_r^{1/2}(b_\perp, \mu)$ emerges from the different soft gluon radiation effects in $\tilde{\Psi}^\pm$ and $\Psi^\pm$ [28]. The mismatch of the rapidity scale ζ and ζ_z can be compensated by the CS kernel $K(b_\perp, \mu)$. Both S and K are independent of the $\pm$ choice. $H^\pm$ is the one-loop perturbative matching kernel [28],

$$\begin{aligned}&H^\pm(\zeta_z, \bar{\zeta}_z, \mu)\\ &= 1 + \frac{\alpha_s C_F}{4\pi}\left(-\frac{5\pi^2}{6} - 4 + \ell_\pm + \bar{\ell}_\pm - \frac{1}{2}(\ell_\pm^2 + \bar{\ell}_\pm^2)\right),\end{aligned} \tag{10}$$

with the abbreviations $\ell_\pm = \ln[(-\zeta_z \pm i\epsilon)/\mu^2]$ and $\bar{\ell}_\pm = \ln[(-\bar{\zeta}_z \pm i\epsilon)/\mu^2]$, the scales $\zeta_z = (2xP^z)^2$ and $\bar{\zeta}_z = (2\bar{x}P^z)^2$, and $\bar{x} = 1 - x$. It should be noticed that $H^\pm$ contains nonzero imaginary parts in $\ell_\pm$ and $\bar{\ell}_\pm$. While the imaginary parts in $\ell_\pm/\bar{\ell}_\pm$ are constants, the ones in the double logarithms $\ell_\pm^2/\bar{\ell}_\pm^2$ are momentum dependent.

A characteristic behavior of Eq. (9) is that this factorization is multiplicative [24], which indicates that hard gluon contributions are local. This is due to the fact that hard gluon exchange between the quark and antiquark sectors in quasi-TMDWFs is power suppressed: if there were such a hard gluon, the spatial separation between its attachments is much smaller than $b_\perp$, resulting in power suppression compared to the typical hard mode contributions. Thus, at leading power, the factorization of quasi-TMDWFs is multiplicative. This feature is illustrated in Fig. 2, in which the collinear, soft, and hard subdiagrams represent the pertinent contributions. Further, ζ_z arising from Lorentz-invariant combinations of collinear momentum modes will provide the natural hard scale of the hard subdiagram. More detailed explanations for the factorization of quasi-TMDPDFs in LaMET are given in the recent review in [27].

D. Collins-Soper kernel from quasi-TMDWFs

From Eq. (9), one can see that the momentum dependence in quasi-TMDWFs provides an option to determine

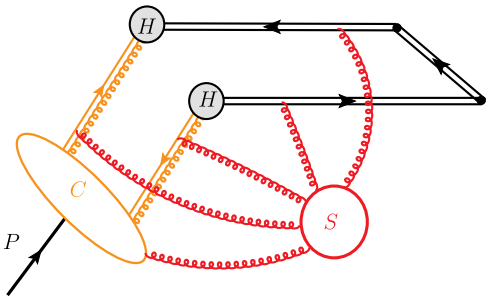

FIG. 2. Leading power reduced graph for pseudoscalar meson quasi-TMDWFs. Here C and S denote the collinear and soft sectors of the infrared structure, while H denotes the hard contributions. Since the hard gluon exchange between the quark and antiquark is power suppressed, the hard parts are disconnected with each others, and therefore the factorization of quasi-WF amplitude is multiplicative.

the CS kernel. This can be written in a way similar to Eq. (1) [28],

$$2\zeta_z\frac{d}{d\zeta_z}\ln\tilde{\Psi}^{\pm}(x,b_\perp,\mu,\zeta_z)=K(b_\perp,\mu)+\frac{1}{2}\mathcal{G}^{\pm}(x^2\zeta_z,\mu)+\frac{1}{2}\mathcal{G}^{\pm}(\bar{x}^2\zeta_z,\mu)+\mathcal{O}\left(\frac{1}{\zeta_z}\right), \quad (11)$$

where $K(b_\perp,\mu)$ denotes the same kernel as in Eq. (1) and does not depend on the hard scale ζ_z for large P^z. Unlike TMDWFs, the quasidistributions also contain hard contributions, whose rapidity dependence is represented by the perturbative $\mathcal{G}^{\pm}$ as a function of hard scale ζ_z. From the ζ_z dependence of quasi-TMDWFs, we can see that, when $P^z\to\infty$, the large logarithms in P^z are partially absorbed into $K(b_\perp,\mu)$ and the remanent is incorporated in the perturbative matching kernel. Therefore, both the matching kernel $H^{\pm}$ and an exponential of the CS kernel $K(b_\perp,\mu)$ are needed to describe the dependence on ζ_z of quasi-TMDWFs.

In order to extract the CS kernel $K(b_\perp,\mu)$ explicitly, one can make use of Eq. (9) with two different large momenta $P_1^z\neq P_2^z\gg 1/b_\perp$ but the same scale ζ_z. Taking a ratio of these two quantities gives

$$\frac{\tilde{\Psi}^{\pm}(x,b_\perp,\mu,P_1^z)}{\tilde{\Psi}^{\pm}(x,b_\perp,\mu,P_2^z)}=\frac{H^{\pm}(xP_1^z,\mu)}{H^{\pm}(xP_2^z,\mu)}\exp\left[K(b_\perp,\mu)\ln\frac{P_1^z}{P_2^z}\right], \quad (12)$$

where the reduced soft function $S_r(b_\perp,\mu)$ and TMDWFs $\Psi^{\pm}(x,b_\perp,\mu,\zeta)$ have been canceled in the ratio. Therefore, the CS kernel $K(b_\perp,\mu)$ can be extracted through

$$K(b_\perp,\mu)=\frac{1}{\ln(P_1^z/P_2^z)}\ln\frac{H^{\pm}(xP_2^z,\mu)\tilde{\Psi}^{\pm}(x,b_\perp,\mu,P_1^z)}{H^{\pm}(xP_1^z,\mu)\tilde{\Psi}^{\pm}(x,b_\perp,\mu,P_2^z)}. \quad (13)$$

Note that the extracted result is formally independent of x and $P_{1/2}^z$ at leading power, and both $\tilde{\Psi}^{+}$ and $\tilde{\Psi}^{-}$ can be used to extract $K(b_\perp,\mu)$. This is derived at the leading power in the factorization scheme and might be undermined by power corrections. Accordingly, in order to reduce the systematic uncertainties, we take the average

$$K(b_\perp,\mu)=\frac{1}{2\ln(P_1^z/P_2^z)}\left[\ln\frac{H^{+}(xP_2^z,\mu)\tilde{\Psi}^{+}(x,b_\perp,\mu,P_1^z)}{H^{+}(xP_1^z,\mu)\tilde{\Psi}^{+}(x,b_\perp,\mu,P_2^z)}+\ln\frac{H^{-}(xP_2^z,\mu)\tilde{\Psi}^{-}(x,b_\perp,\mu,P_1^z)}{H^{-}(xP_1^z,\mu)\tilde{\Psi}^{-}(x,b_\perp,\mu,P_2^z)}\right]. \quad (14)$$

The details will be discussed in Sec. III E.

III. NUMERICAL SIMULATIONS AND RESULTS

In this section, we present our lattice QCD results. We start with the lattice setup, followed by results for quasi-TMDWFs with two-point correlations. The Wilson loop results are discussed in Sec. III C. Section III D studies the operator mixing effects. Our main result on the CS kernel is presented in Sec. III E. Section III F includes some overall discussions.

A. Lattice setup

Our numerical simulations use $N_f=2+1+1$ valence clover fermions on a highly improved staggered quark sea [42] and a one-loop Symanzik improved gauge action [43], generated by the MILC Collaboration [44] using periodic boundary conditions. In the calculations, we use a single ensemble with the lattice spacing $a\simeq 0.12$ fm and the volume $n_s^3\times n_t=48^3\times 64$ at physical sea-quark masses. In order to increase the signal-to-noise ratio, we tune the light-valence quark masses to the strange-quark one, namely, $m_\pi^{\rm sea}=130$ and $m_\pi^{\rm val}=670$ MeV, which could generate some nonunitarity effects. On the other hand, the Collins-Soper kernel only depends weakly on quark mass, and we may consider that valence quarks are strangelike, namely, the hadrons involved are kaons.

To further improve the statistical signals, we adopt hypercubic (HYP) smeared fat links [45] for the gauge ensembles. To access the large-momentum limit for the CS kernel, we employ three different hadron momenta as $P^z=2\pi/n_s\times\{8,10,12\}=\{1.72,2.15,2.58\}$ GeV corresponding to the boost factor $\gamma=\{2.57,3.21,3.85\}$.

B. Quasi-TMDWFs from two-point correlators

In order to calculate the quasi-TMDWFs defined in Eq. (4), we generate Coulomb-gauge wall-source propagators,

$$S_w(x,t,t';\vec{p})=\sum_{\vec{y}}S(t,\vec{x};t',\vec{y})e^{i\vec{p}\cdot(\vec{y}-\vec{x})}, \quad (15)$$

where $(t',\vec{y})$ and $(t,\vec{x})$ denote the space-time positions of source and sink. Then one can construct the two-point function related to the quasi-TMDWFs in Eq. (4),

$$C_2^{\pm}(z,b_\perp,P^z;p^z,L,t)=\frac{1}{n_s^3}\sum_{\vec{x}}\mathrm{tr}e^{i\vec{P}\cdot\vec{x}}\langle S_w^{\dagger}(\vec{x}_1,t,0;-\vec{p})\times\Gamma U_{\square,\pm L}(\vec{x}_1,\vec{x}_2)S_w(\vec{x}_2,t,0;\vec{p})\rangle, \quad (16)$$

with $\vec{x}_1=\vec{x}+z\hat{n}_z/2+b_\perp\hat{n}_\perp$ and $\vec{x}_2=\vec{x}-z\hat{n}_z/2$. The quark momentum $\vec{p}=(\vec{0}_\perp,p^z)$ is along the z direction, and each of two quarks carries half of the hadron momentum. Thereby, the hadron momentum satisfies $\vec{P}=2\vec{p}$. The antiquark propagator can be obtained from Eq. (10) by applying γ_5-hermiticity $S_w(x,y)=\gamma_5 S_w(y,x)^{\dagger}\gamma_5$. As mentioned above, the Dirac structures are chosen as $\Gamma=\gamma^z\gamma_5$

and $\gamma^t\gamma_5$ that can be projected onto the leading-twist light-cone contributions in the large-P^z limit.

By generating the wall-source propagators with quark momenta $p^z = \pm\{4, 5, 6\} \times 2\pi/(n_s a)$ and three segments of gauge links following Eq. (6), one can construct the two-point correlation functions on the lattice. With the help of reduction formulas, the $C_2^{\pm}$ can be parametrized as

$$C_2^{\pm}(z, b_\perp, P^z; p^z, L, t) = \frac{A_w(p^z)A_p}{2E}\tilde{\Phi}^{\pm 0}(z, b_\perp, P^z, L) \times e^{-Et}[1 + c_0(z, b_\perp, P^z, L)e^{-\Delta E t}], \tag{17}$$

where $A_w(p^z)$ is the matrix element of the pseudoscalar meson interpolating field with Coulomb-gauge fixed wall source and A_p is the one for a point source (sink). These terms, as well as the factor $E^{-1} = 1/\sqrt{m_\pi^2 + (P^z)^2}$, are canceled by the local two-point function $C_2^{\pm}(0, 0, P^z; p^z, 0, t)$ at the same time slice. Thus, the remaining ground-state matrix element $\tilde{\Phi}^{\pm 0}$ is normalized. The ratio of nonlocal and local two-point functions can be parametrized as

$$\begin{aligned} R^{\pm}(z, b_\perp, P^z, L, t) &= \frac{C_2^{\pm}(z, b_\perp, P^z, L, t)}{C_2(0, 0, P^z, 0, t)} \\ &= \tilde{\Phi}^{\pm 0}(z, b_\perp, P^z, L)[1 + c_0(z, b_\perp, P^z, L)e^{-\Delta E t}], \end{aligned} \tag{18}$$

where C_2 in the denominator is a local correlator.

In the above parametrization, the excited-state contributions are collected into the c_0 term, and ΔE denotes the mass gap between the ground and first excited state. With the increase of Euclidean time, contributions from the excited state decay and the plateau obtained for $R^{\pm}(z, b_\perp, P^z, L, t)$ at large times reflects the ground-state contribution $\tilde{\Phi}^{\pm 0}$. We employ two methods to extract $\tilde{\Phi}^{\pm 0}$, namely, the two-state fit directly using Eq. (18) and the one-state fit by setting $c_0 = 0$. With a large enough Euclidean time, Fig. 3 exhibits a comparison using two methods for the case with small $\{z, b_\perp\}$. From this figure, one can see that the one-state fit result is consistent with the two-state fit one but gives a more conservative error estimate. The two-state fit works at $t \in [2a, 8a]$ and the one-state fit works at the plateau region $t \in [5a, 8a]$, whereas the excited-state contamination would dominate for the two-state fit in a very high precision, especially for the cases with large $\{z, b_\perp\}$. So with current accuracy, we adopt the more conservative results from the one-state fit in the following analysis. More details can be found in Appendix A.

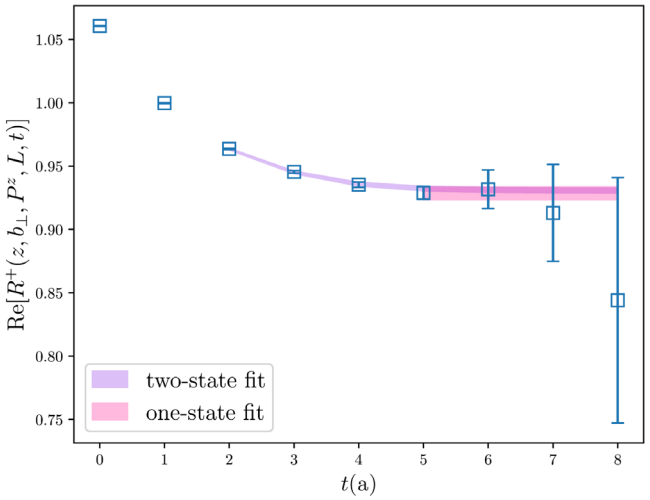

FIG. 3. Comparison of two-state fit and one-state fit to extract $\tilde{\Phi}^{\pm 0}(z, b_\perp, P^z, L)$. Taking $\{z, b_\perp, P^z, L\} = \{0a, 2a, 24\pi/n_s, 6a\}$ as example, we can see that the two-state fit works for $t \in [2a, 8a]$ while the one-state fit works for $t \in [5a, 8a]$. The fitted results are consistent with each other, while the one-state fit is more conservative.

C. Wilson loop renormalization

The unsubtracted quasi-TMDWF matrix elements $\tilde{\Phi}^{\pm 0}(z, b_\perp, P^z, a, L)$ extracted from the joint fit of the two-point function contain a factor $e^{-\delta\bar{m}(2L+b_\perp)}$ from the linear divergence, the heavy quark effective potential factor $e^{-V(b_\perp)L}$, and logarithmic divergences Z_O,

$$\tilde{\Phi}^{\pm 0}(z, b_\perp, P^z, a, L) \propto e^{-\delta\bar{m}(2L+b_\perp)}e^{-V(b_\perp)L}Z_O, \tag{19}$$

where Z_O has logarithmic dependence on lattice spacing a.

The linear divergence in $e^{-\delta\bar{m}(2L+b_\perp)}$ comes from the self-energy of the Wilson line [46–49], where $\delta\bar{m}$ contains a term proportional to $1/a$ and a nonperturbative renormalon contribution m_0,

$$\delta\bar{m} = \frac{m_{-1}(a)}{a} - m_0. \tag{20}$$

Note that the exponent of the linear divergence term is proportional to the total length of the Wilson link, e.g., $2L + b_\perp$ for the staple link. Because of this factor, the numerical value for a Wilson loop dramatically decreases for small a and large L.

The heavy quark effective potential term $e^{-V(b_\perp)L}$ comes from interactions between the two Wilson lines along the z direction in the staple link. The heavy quark effective potential $V(b_\perp)$ is often used to determine the lattice spacing of an ensemble.

The logarithmic divergence Z_O comes from the vertices involving the Wilson line and light quark. The logarithmic divergence up to leading order, resummed by the renormalization group equation and matched to the $\overline{\mathrm{MS}}$ scheme, is [50,51]

$$Z_O(1/a,\mu) = \left(\frac{\ln[1/(a\Lambda_{\rm QCD}^{\rm latt})]}{\ln[\mu/\Lambda_{\rm QCD}^{\overline{\rm MS}}]}\right)^{\frac{3C_F}{b_0}}, \tag{21}$$

where $\Lambda_{\rm QCD}^{\rm latt}$ is different from that in the $\overline{\rm MS}$ scheme. One can use both to effectively absorb higher-order contributions [52].

In this work, the Wilson loop renormalization method [48,53–56] is adopted, in which the Wilson loop Z_E defined in Eq. (8) contains linear divergence and heavy quark effective potential,

$$Z_E(2L, b_\perp, a) \propto e^{-\delta\bar{m}(4L+2b_\perp)} e^{-V(b_\perp)2L}. \tag{22}$$

According to Ref. [51], $\delta\bar{m}$ in the Wilson loop is the same as that in hadron matrix elements, and thus it is anticipated that the linear divergence is removed when dividing by $\sqrt{Z_E(2L, b_\perp, a)}$,

$$\tilde{\Phi}^{\pm}(z, b_\perp, P^z, a, L) = \frac{\tilde{\Phi}^{\pm 0}(z, b_\perp, P^z, a, L)}{\sqrt{Z_E(2L, b_\perp, a)}}. \tag{23}$$

As shown in Fig. 4, the subtracted quasi-TMDWFs tend to be a constant when $L \geq 0.4$ fm. We then use the subtracted quasi-TMDWFs defined as

$$\tilde{\Phi}^{\pm}(z, b_\perp, P^z, a) = \lim_{L\to\infty} \frac{\tilde{\Phi}^{\pm 0}(z, b_\perp, P^z, a, L)}{\sqrt{Z_E(2L, b_\perp, a)}}. \tag{24}$$

However, it is anticipated that there is a residual logarithmic divergence Z_O,

$$\frac{\tilde{\Phi}^{\pm 0}(z, b_\perp, P^z, a, L)}{\sqrt{Z_E(2L, b_\perp, a)}} \propto \frac{e^{-\delta\bar{m}(2L+b_\perp)} e^{-V(b_\perp)L} Z_O}{e^{-\delta\bar{m}(2L+b_\perp)} e^{-V(b_\perp)L}} = Z_O. \tag{25}$$

In the extraction of the CS kernel, a ratio of quasi-TMDWFs is adopted and accordingly the residual logarithmic divergence Z_O is canceled.

D. Power correction effects with different operators

For a pseudoscalar meson on a Euclidean lattice, both $\Gamma = \gamma^t\gamma_5$ and $\gamma^z\gamma_5$ project onto the leading-twist light-cone distribution amplitude, i.e., $\gamma^+\gamma_5$ in the large-P^z limit. The differences between them arises from power corrections in terms of $M^2/(P^z)^2$.

Figure 5 shows the comparison of the $\lambda = zP^z$ dependence of quasi-TMDWFs with $\Gamma = \gamma^t\gamma_5$ and $\gamma^z\gamma_5$ at $P^z = 24\pi/n_s \simeq 2.58$ GeV. It can be seen from the plots that there are some differences between the two sets of results for the real part in the small-λ region. The differences are expected to decrease with increasing P^z, and the correlators with $\gamma^t\gamma_5$ and $\gamma^z\gamma_5$ will gradually converge to the light-cone from opposite directions. In addition, in light-cone coordinates, γ^t and γ^z can be represented by γ^+ and γ^-,

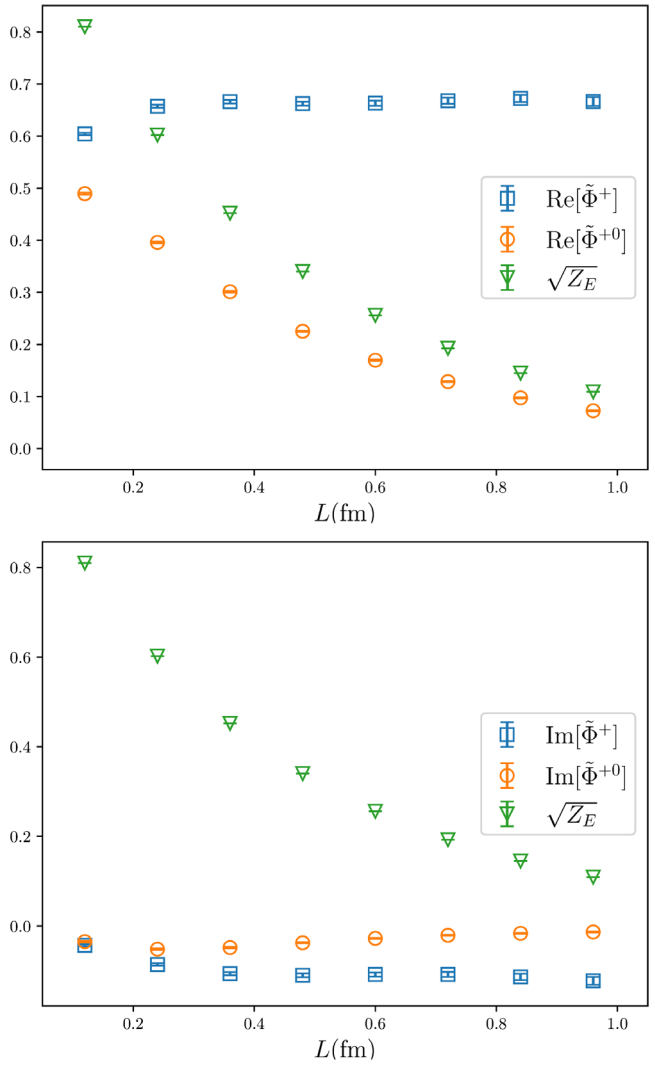

FIG. 4. Results for the L dependence of unsubtracted and subtracted quasi-TMDWFs: real part (upper) and imaginary part (lower), as well as the square root of the Wilson loop. The cases $\Gamma = \gamma^z\gamma_5$ and $\{P^z, b_\perp, z\} = \{16\pi/n_s, 2a, 2a\}$ are used for illustration.

$$\gamma^t\gamma_5 = \frac{1}{\sqrt{2}}(\gamma^+ + \gamma^-)\gamma_5,$$
$$\gamma^z\gamma_5 = \frac{1}{\sqrt{2}}(\gamma^+ - \gamma^-)\gamma_5. \tag{26}$$

Because of the momentum along the light-cone, operators with $\gamma^-\gamma_5$ correspond to higher-order terms of TMDWFs. Therefore, power corrections arising from finite P^z are likely to be eliminated in the average of these two terms,

$$\tilde{\Phi}^{\pm} = \frac{1}{2}[\tilde{\Phi}^{\pm}(\Gamma = \gamma^t\gamma_5) + \tilde{\Phi}^{\pm}(\Gamma = \gamma^z\gamma_5)]. \tag{27}$$

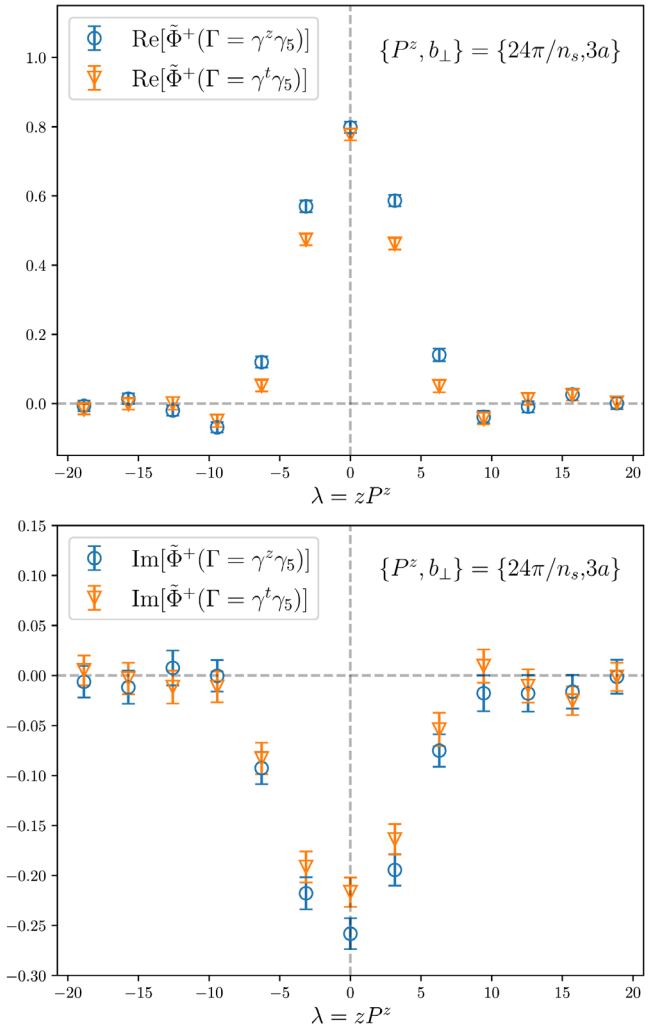

FIG. 5. λ dependence of quasi-WF matrix elements with different Dirac structures. Here we take the case of $\{P^z, b_\perp\} = \{24\pi/n_s, 3a\}$ as an example; the deviation between these two cases mainly comes from power corrections. Results for more sets of $\{P^z, b_\perp\}$ are shown in Appendix C.

For a quantitative analysis, see the appendix of [31]. In Appendix C, we also estimate that the power correction here reaches order 5%, which agrees with the conclusion in Ref. [31]. We take this power correction effect as one possible source of systematic uncertainties in the following analysis.

According to our numerical simulations, the subtracted quasi-TMDWFs in coordinate space $\tilde{\Phi}^\pm(z, b_\perp, P^z)$ as a function of $\lambda = zP^z$ are complex, which is shown in Fig. 6. The examples are the real and imaginary part of $\tilde{\Psi}^\pm(x, b_\perp, P^z)$ with $P^z = 24\pi/n_s$, $b_\perp = 2a$, and $4a$. To determine quasi-TMDWFs in momentum space $\tilde{\Psi}^\pm(x, b_\perp, P^z)$, we use a Fourier transformation (FT),

$$\tilde{\Psi}^\pm(x, b_\perp, P^z) = \frac{1}{2\pi}\sum_{-z_{\max}}^{z_{\max}} e^{ixzP^z}\tilde{\Phi}^\pm(z, b_\perp, P^z), \quad (28)$$

where $z = \pm z_{\max}(z_{\max} > 0)$ reaches the boundary of our data. Because of the imaginary part of $\tilde{\Phi}^\pm(z, b_\perp, P^z)$, $\tilde{\Psi}^\pm(x, b_\perp, P^z)$ also has an imaginary part. We obtain the quasi-TMDWFs in momentum space for both real and imaginary parts of $\tilde{\Psi}^\pm(x, b_\perp, P^z)$ shown in Fig. 7 by taking $P^z = 24\pi/n_s$, $b_\perp = 2a$, and $4a$ as examples. We truncate the FT at $-z_{\max}$ and $z_{\max}$. The deviation of $\tilde{\Phi}^\pm(\pm z_{\max}, b_\perp, P^z)$ from zero is a measure of the resulting truncation error. For the largest range of z values we could realize numerically, $z_{\max} = 1.44$ fm, this error is still noticeable. This brute-force truncation of the FT leads to oscillatory behavior of the TMDWFs. This oscillation in $\tilde{\Phi}(x, b_\perp, P^z)$ can be eliminated by an appropriate extrapolation for $\tilde{\Phi}(z, b_\perp, P^z)$ as a function of zP^z before Fourier transformation. While the signal-to-noise ratio of our data is not smooth enough, the brute-force Fourier transformation is adopted. More details can be found in Appendix D.

E. Collins-Soper kernel from quasi-TMDWFs

The CS kernel governs the rapidity evolution and thus is independent of the momentum fraction of the involved parton. But as indicated in Eq. (9), the factorization formula works only when $xP^z \gg \Lambda_{\mathrm{QCD}}$ and could be invalid in the end-point regions $x \to 0, 1$. Power corrections are presumably of the form $1/(xP^z)^2$ or $1/(\bar{x}P^z)^2$ [24,28]. Therefore, the numerical CS kernel is fitted by a function of x, P_1^z, and P_2^z and is written as $K(b_\perp, \mu, x, P_1^z, P_2^z)$,

$$\begin{aligned} &K(b_\perp, \mu, x, P_1^z, P_2^z) \\ &= \frac{1}{2\ln(P_1^z/P_2^z)}\left[\ln\frac{H^+(xP_2^z, \mu)\tilde{\Psi}^+(x, b_\perp, \mu, P_1^z)}{H^+(xP_1^z, \mu)\tilde{\Psi}^+(x, b_\perp, \mu, P_2^z)}\right. \\ &\left. + \ln\frac{H^-(xP_2^z, \mu)\tilde{\Psi}^-(x, b_\perp, \mu, P_1^z)}{H^-(xP_1^z, \mu)\tilde{\Psi}^-(x, b_\perp, \mu, P_2^z)}\right]. \end{aligned} \quad (29)$$

Here $K(b_\perp, \mu, x, P_1^z, P_2^z)$ are extracted from the perturbative matching kernels and quasi-TMDWFs using one-loop matching. They will have power corrections of the form $\mathcal{O}(1/(xP^z)^2)$ and $\mathcal{O}(1/(\bar{x}P^z)^2)$. In order to extract the leading power contributions, we adopt the following parametrization:

$$\begin{aligned} &K(b_\perp, \mu, x, P_1^z, P_2^z) \\ &= K(b_\perp, \mu) + A\left[\frac{1}{x^2(1-x)^2(P_1^z)^2} - \frac{1}{x^2(1-x)^2(P_2^z)^2}\right], \end{aligned} \quad (30)$$

where A is the coefficient accounting for the leading higher power contributions and can be determined through a joint fit, which is performed by combining the lattice data for the two different momenta in the regions not so close to $x = 0, 1$ for each $b_\perp$.

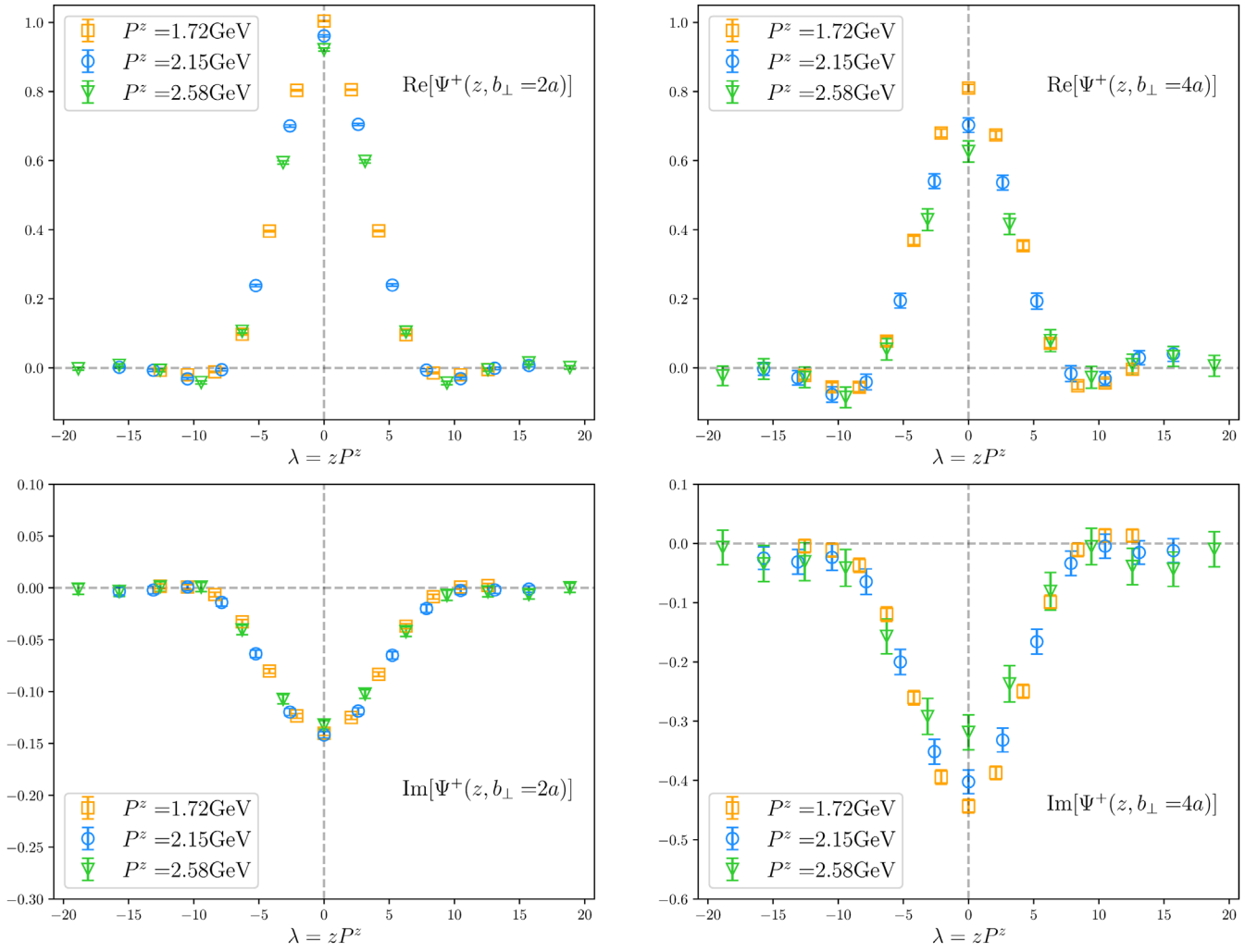

FIG. 6. Examples for subtracted quasi-TMDWFs in coordinate space. Here we take the cases of $P^z = \{16, 20, 24\}\pi/n_s$. According to our results, the subtracted quasi-TMDWFs $\tilde{\Phi}^+(z, b_\perp, P^z)$ are complex, thus the real and imaginary parts both need to be investigated. The upper four figures are for subtracted quasi-TMDWFs $\tilde{\Phi}^+(z, b_\perp, P^z)$ as a function of $\lambda = zP^z$ after the average over the two Dirac structures ($\gamma^t\gamma_5$ and $\gamma^z\gamma_5$) is taken. The upper left figure shows the real part of $\tilde{\Phi}^+(z, b_\perp, P^z)$ with $b_\perp = 2a$, while the upper right one is for $\tilde{\Phi}^+(z, b_\perp, P^z)$ with $b_\perp = 4a$. The lower two figures show the corresponding imaginary parts with $b_\perp = 2a$ and $4a$.

Figure 8 presents the physical CS kernel $K(b_\perp, \mu)$ with $b_\perp = \{0.12, 0.24, 0.36, 0.48, 0.60\}$ fm. By employing three cases of quasi-TMDWFs with $P^z = \{8, 10, 12\} \times 2\pi/n_s$, one can extract $K(b_\perp, \mu, x, P_1^z, P_2^z)$ with $P_1^z/P_2^z = 10/8$ and $12/8$, shown as the different colored bands. Except for in the end-point regions ($x < 0.2$ or $x > 0.8$), the lattice data are flat and reflect the leading power contribution, which conforms with expectations. Using the parametrization formula (30), the physical CS kernel $K(b_\perp, \mu)$ can be determined by fitting the data, shown as the green band. Additionally, we have also verified the consistency of different end-point regions, as well as parametrization equations. More details can be found in Appendix E. As mentioned before, at large $b_\perp$, the quasi-TMDWFs show oscillations due to the truncation of the Fourier transformation, which also affects the extracted $K(b_\perp, \mu, x, P_1^z, P_2^z)$, as shown in the lower panel of Fig. 8. This oscillation effect can be, in principle, removed once larger z data become possible, or if one knows how to extrapolate the current data to the larger z or λ region.

Theoretically, the physical CS kernel is purely real; however, there still exists a residual imaginary part at one-loop matching. Based on the perturbative results given in Ref. [28], one can notice that both the TMDWFs and quasi-TMDWFs contain an explicit imaginary contribution. The matching kernel between them describes the ultraviolet difference between these two quantities, and thus the complex phase in the matching kernel arises from the difference in the imaginary parts of TMDWFs and quasi-TMDWFs. From the expression of the matching kernel in Eq. (10), one can see that the imaginary parts arise from the $\ln(-\zeta_z \pm i\epsilon)$ and $\ln^2(-\zeta_z \pm i\epsilon)$ terms.

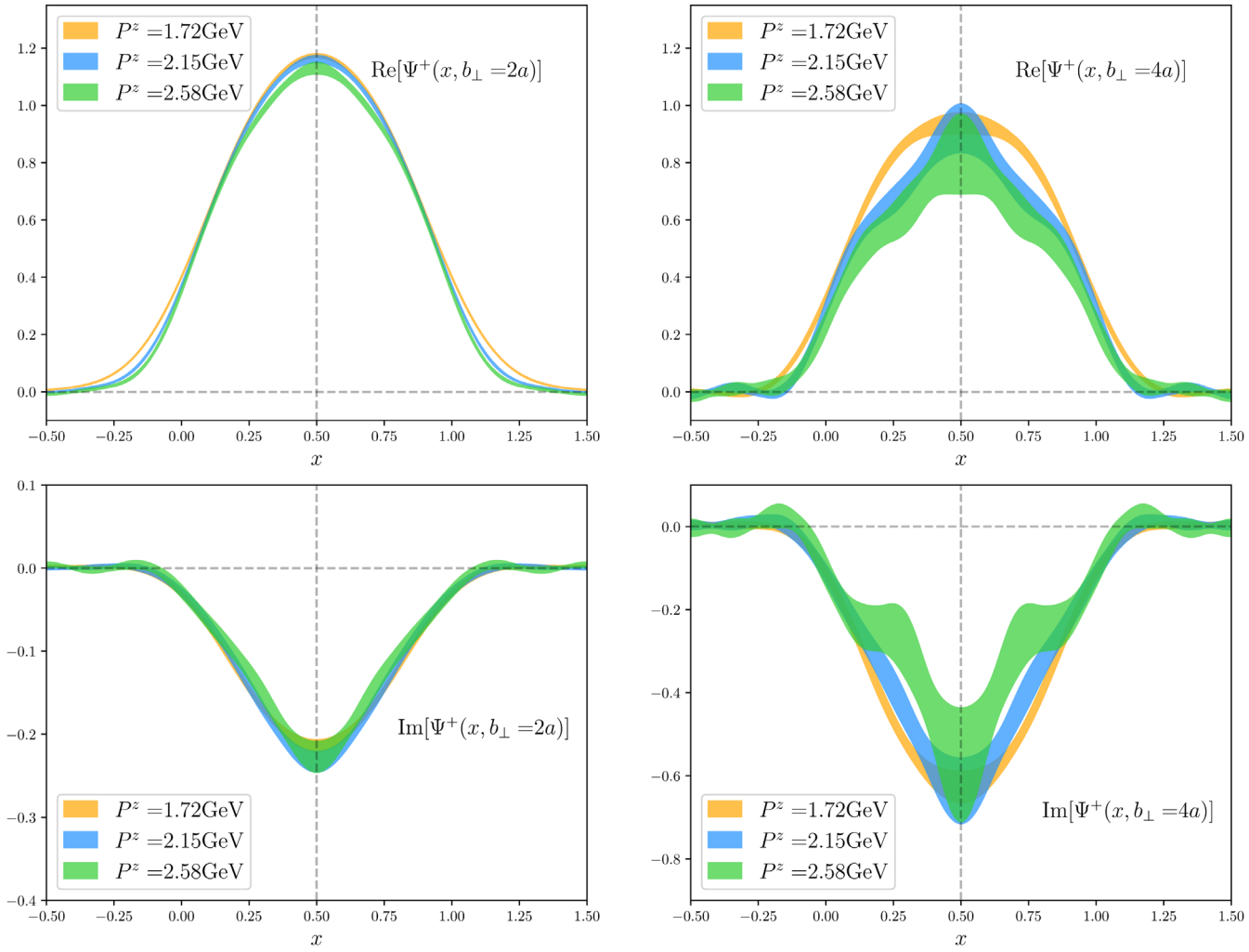

FIG. 7. Examples for subtracted quasi-TMDWFs in momentum space with hadron momentum $P^z = 24\pi/n_s$. The subtracted quasi-TMDWFs in momentum space $\tilde{\Psi}^+(x, b_\perp, P^z)$ are Fourier transformed from $\tilde{\Phi}^+(z, b_\perp, P^z)$, which have real and imaginary parts. Both have to be investigated. Shown in Eq. (28), a brute-force FT is used to determine $\tilde{\Psi}^+(x, b_\perp, P^z)$, where $z_{\min} = -1.44$, $z_{\max} = 1.44$ fm. The upper left figure shows the real part for $\tilde{\Psi}^+(x, b_\perp, P^z)$ with the $b_\perp = 2a$ case, while the upper right one is for $\tilde{\Psi}^+(x, b_\perp, P^z)$ with the $b_\perp = 4a$ case. Correspondingly, the lower two figures show the imaginary part for $\tilde{\Psi}^+(x, b_\perp, P^z)$ with $b_\perp = 2a$ and $4a$.

The second term is momentum dependent, and thus taking a ratio of hard kernels with different momentum will not remove the imaginary part.

On the lattice side, we have found that the quasi-TMDWFs are indeed complex. However, when taking the ratio of quasi-TMDWFs with different momentum, the imaginary parts mostly cancel. As a result, this leaves a mismatch between the imaginary parts of the perturbative matching kernel and quasi-TMDWFs, though both are complex. Shown as Fig. 9, almost all of the imaginary parts come from the ratios of perturbative kernels. This mismatch of imaginary parts is puzzling, and we guess it might come from lattice artifacts or missing higher power or radiative corrections.

For now, we can only consider this imaginary part as systematic uncertainty of our final results, and it can be expressed as

$$\sigma_{\text{sys}} = \sqrt{K(b_\perp, \mu) + \text{Im}^2[K^+(b_\perp, \mu)]} - K(b_\perp, \mu), \tag{31}$$

where $\text{Im}[K^+(b_\perp, \mu)]$ represents the numerical imaginary part of extracting $K(b_\perp, \mu)$ only by $\tilde{\Psi}^+$,

$$K^\pm(b_\perp, \mu) = \frac{1}{\ln(P_1^z/P_2^z)} \ln \frac{H^\pm(xP_2^z, \mu)\tilde{\Psi}^\pm(x, b_\perp, \mu, P_1^z)}{H^\pm(xP_1^z, \mu)\tilde{\Psi}^\pm(x, b_\perp, \mu, P_2^z)}. \tag{32}$$

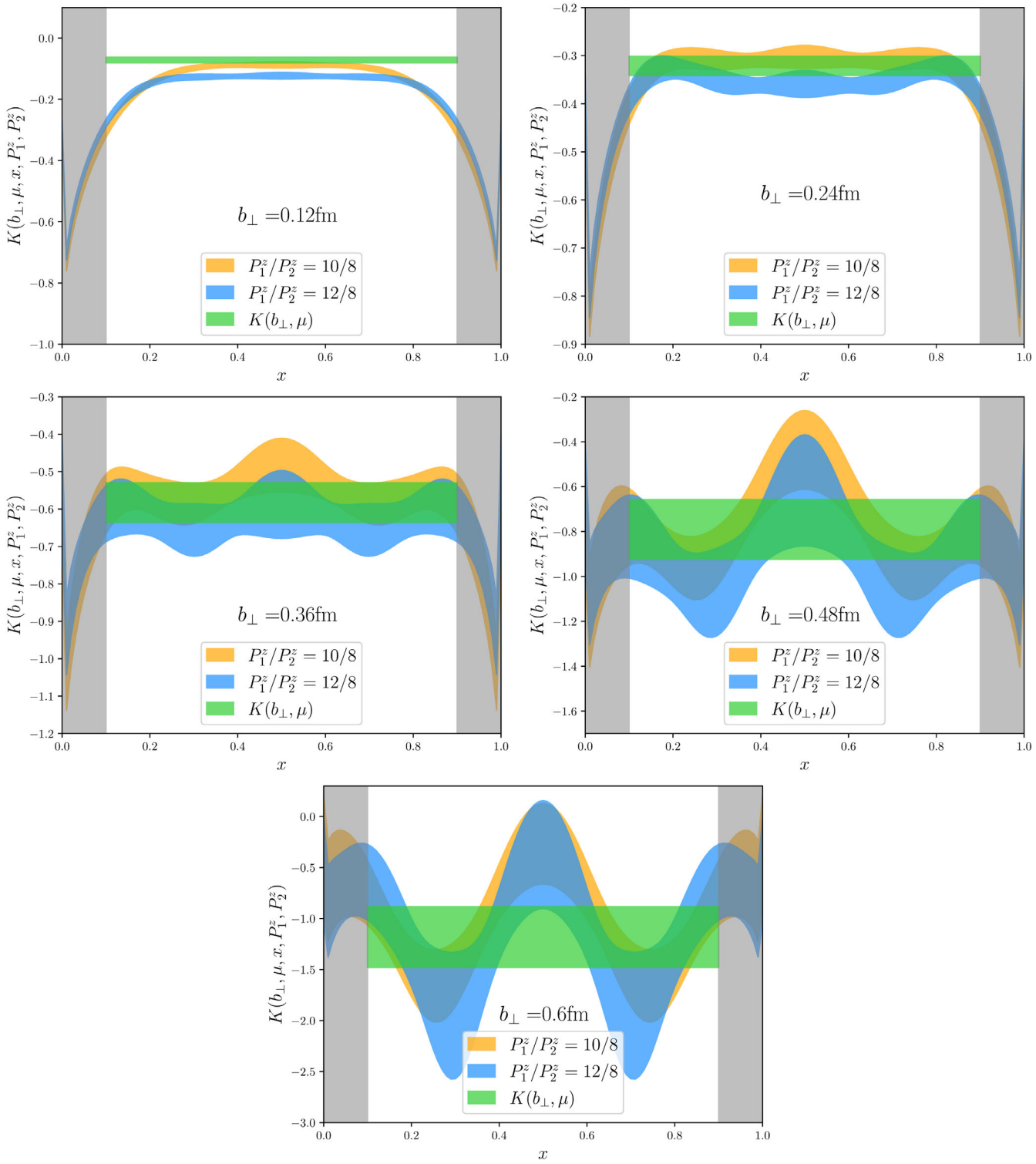

FIG. 8. The fit results of $K(b_\perp, \mu, x, P_1^z, P_2^z)$ extracted from the quasi-WFs $\tilde{\Psi}^\pm$. The chosen momentum pairs $\{P_1^z, P_2^z\}$ are denoted by P_1^z/P_2^z in the legend. The figures correspond to cases with $b_\perp = \{0.12, 0.24, 0.36, 0.48, 0.60\}$ fm. The horizontal shaded band shows the central value and uncertainty of $K(b_\perp, \mu)$, as well as the fit range of x, as described in the text. In the large-$b_\perp$ area, the strong oscillation exists in the shaded area at both edges, where the LaMET approach is invalid and is caused by the breakdown of the large-momentum expansion.

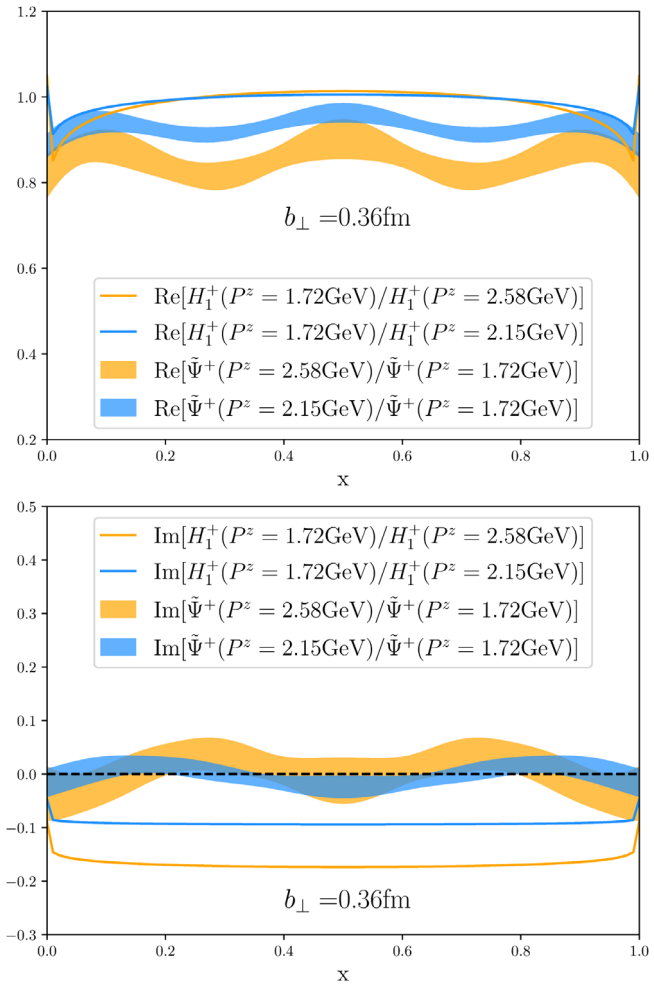

FIG. 9. Comparison of ratios of one-loop matching kernels and quasi-TMDWFs with $P_1^z/P_2^z = 2.58/1.72$ and $2.15/1.72$ GeV, respectively. Lower: points out the sources of imaginary parts in the CS kernel.

It should be noticed that the perturbative matching kernel $H^+(zP^z,\mu)$ is the complex conjugate of $H^-(zP^z,\mu)$; that is, the imaginary parts in these terms can cancel each other when we employ the average of $H^+(zP_2^z,\mu)/H^+(zP_1^z,\mu)$ and $H^-(zP_2^z,\mu)/H^-(zP_1^z,\mu)$. Therefore, as the final result, we adopt $K(b_\perp,\mu) = [K^+(b_\perp,\mu) + K^-(b_\perp,\mu)]/2$ to reserve the real part and regard the imaginary contributions as our systematic uncertainty.

F. Results and discussions

One should notice that the Wilson loop renormalized quasi-TMDWF on the lattice [Eq. (24)] has a scale dependence on a. If one converts it to the $\overline{\text{MS}}$ scheme through dividing it by Z_O [Eq. (21)], the scale μ is introduced. In principle, one should convert the Wilson loop renormalized quasi-TMDWF to the $\overline{\text{MS}}$ scheme since our factorization formula works there. However, since Z_O has no dependence on momentum P_z, it cancels in the ratio of quasi-TMDWFs, and so does the scale dependence. So, one does not need to do the scheme and scale conversion of the quasi-TMDWF during the extraction of the CS kernel.

The extracted CS kernel from the combined fit of the ratios of quasi-TMDWFs with different momenta are shown as the red data points in Fig. 10. In this figure, we exhibit two kinds of errors for $K(b_\perp,\mu)$, in which the smaller ones denote statistical uncertainties, while the larger ones include both statistical and systematical uncertainties. In the small-$b_\perp$ region, the systematic uncertainties are dominant due to

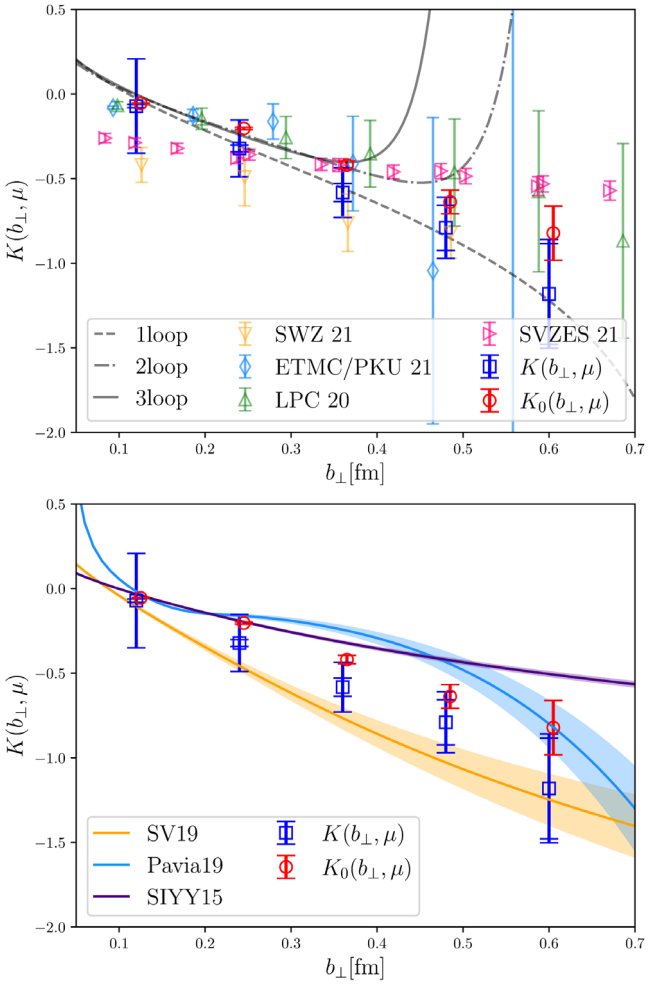

FIG. 10. Upper: comparison of our results $K(b_\perp,\mu)$ and $K_0(b_\perp,\mu)$ with the lattice calculations by Shanahan *et al.* [34], the Lattice Parton Collaboration [31], European Twisted Mass Collaboration/Peking University [33], and Schlemmer *et al.* [32], as well as the perturbative calculations up to three loops. $K(b_\perp,\mu)$ denotes the CS kernel extracted through one-loop matching, whose uncertainties correspond to the statistical errors and the systematic ones from the nonzero imaginary part. $K_0(b_\perp,\mu)$ denotes our tree-level results, only with statistical uncertainties. Lower: comparison of our result with phenomenological extractions: Scimemi and Vladimirov [19], Pavia19 [20], and Sun *et al.* [15] give phenomenological parametrizations of the CS kernel fitted to data from high energy collision processes like Drell-Yan.

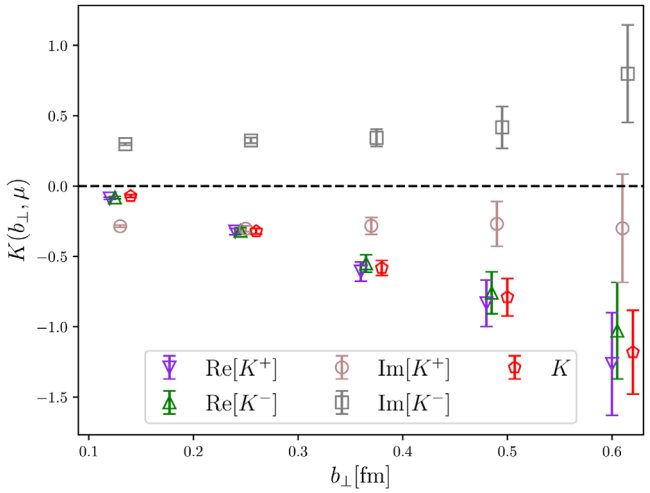

FIG. 11. Comparison of the Collins-Soper kernel K, as well as $\mathrm{Re}K^{\pm}$ and $\mathrm{Im}K^{\pm}$ with $b_\perp$.

the corrections from power correction effects and nonzero imaginary parts.

As mentioned above, the imaginary parts might come from higher-order/power corrections in the matching kernel, and here we consider them as one possible source of systematical uncertainties. In practice, we use the average of K^+ and K^- as our final result and estimate the systematical uncertainties by the deviations between the average and $K^+(K^-)$. We also compare the Collins-Soper kernel K with $\mathrm{Re}[K^{\pm}]$ and $\mathrm{Im}[K^{\pm}]$ in Fig. 11. As shown in the figure, the imaginary parts are independent of $b_\perp$.

As a comparison, we also give the tree-level matching result for the CS kernel. With the leading order matching kernel $H(xP^z,\mu) = 1 + \mathcal{O}(\alpha_s)$, Eq. (13) simplifies to the ratio of quasi-TMDWFs $\tilde{\Phi}$ at $z = 0$ with momentum P_1^z/P_2^z. The blue dots in Fig. 10 denote the results obtained for tree-level matching, for which only statistical uncertainties are shown.

We compare our results with the ones from perturbative calculations and phenomenological extractions, as well as the lattice results determined by other collaborations.

The black solid and dashed lines in the upper panel of Fig. 10 indicate the perturbative results up to three loops, with a running coupling constant $\alpha_s(\mu = 1/b_\perp)$. The perturbative calculations work well in the small-$b_\perp$ region ($b_\perp \ll 1/\Lambda_{\mathrm{QCD}}$), while they will diverge with $b_\perp$ increasing. In contrast, the lattice calculation will give accurate predictions in the nonperturbative region, whereas, due to the power corrections, it might suffer large systematic uncertainties in the small-$b_\perp$ region.

Similar to this work, the results of LPC [31] and ETMC/PKU [33] are also extracted from quasi-TMDWFs through a tree-level matching. Adopting the one-loop matching formula, as well as considering the operator mixing effects, will help one to reduce the systematic uncertainties and obtain more precise results. In addition, considering the different directions of the gauge link will help us to eliminate the contributions from the unphysical imaginary part and then improve the accuracy of our results.

In another way, the SWZ [34] and SVZES [32] results are obtained from quasi-TMDPDFs. Compared with the complicated nucleon correlation functions, the meson ones are much easier to obtain better signals. In addition, the wave functions of the meson are nearly symmetric in x space, thereby making it more convenient to parametrize the oscillation effects and obtain the physical results in the large-P^z limit as in Fig. 8. In addition, the light meson makes it easier to reach a larger boosted factor; as one can see from the small-$b_\perp$ region, the results from quasi-TMDWFs fit well with the perturbative calculations compared to the ones from quasi-TMDPDFs.

The lower panel of Fig. 10 shows the comparison with phenomenological results. SV19 [19] and SIYY15 [15] use a parametrization with perturbative and nonperturbative parts. However, Pavia19 [20] obtained their result with the factorization of TMDPDFs, obtaining the CS kernel from the rapidity derivative. In addition, they fit parameters from the Drell-Yan data to obtain their phenomenological CS kernel. The results from different methods exhibit obvious inconsistency in the nonperturbative region. Our result shows a better consistency with SV19.

IV. SUMMARY AND OUTLOOK

In this work, we have calculated the CS kernel on a MILC lattice configuration in the large-momentum effective theory framework. Comparing with our previous study [31], the one-loop matching kernel has been adopted in this study, and several hadron momenta were used to extract the CS kernel. We found that, in the small-$b_\perp$ region, our results are consistent with perturbative QCD. In the large-$b_\perp$ region, our results seem consistent with other lattice calculations in the literature within uncertainties.

For our future studies, we need to use lattice configurations with multiple lattice spacing to understand the finite lattice spacing effects. We would use a valence quark mass consistent with the sea-quark one to reduce the nonunitarity effects. One such effect might be the imaginary part of the meson wave function, which seems inconsistent with perturbative calculation at the present time. Clearly, all these explorations will take more computational resources.

ACKNOWLEDGMENTS

We thank Xu Feng, Yizhuang Liu, and Feng Yuan for useful discussions. This work is supported in part by Natural Science Foundation of China under Grants No. 11735010, No. 11911530088, No. U2032102, No. 11653003, No. 11975127, No. 11975051, No. 12005130, and No. 12147140. M. C., J. H., and W. W. are also supported by Natural Science Foundation of Shanghai under Grant

No. 15DZ2272100. P. S. is also supported by the Jiangsu Specially Appointed Professor Program. Y. B. Y. is also supported by the Strategic Priority Research Program of Chinese Academy of Sciences, Grants No. XDB34030303 and No. XDPB15. A. S., P. S., W. W., Y. B. Y., and J. H. Z. are also supported by the NSFC-DFG joint grant under Grants No. 12061131006 and No. SCHA 458/22. X. J. is partially supported by the U.S. Department of Energy under Award No. DE-SC0020682. The calculation was supported by Advanced Computing East China Subcenter and the π2.0 cluster at the Center for High Performance Computing, Shanghai Jiao Tong University.

APPENDIX A: EUCLIDEAN TIME t DEPENDENCE OF NORMALIZED C_2

In Sec. III B, the ratio of nonlocal and local two-point functions is parametrized in Eq. (18),

$$R^{\pm}(z, b_\perp, P^z, L, t) = \frac{C_2^{\pm}(z, b_\perp, P^z, L, t)}{C_2(0, 0, P^z, 0, t)} = \tilde{\Phi}^{\pm 0}(z, b_\perp, P^z, L)[1 + c_0(z, b_\perp, P^z, L)e^{-\Delta E t}]. \quad \text{(A1)}$$

From the above equation, one can see that $R^{\pm}(z, b_\perp, P^z, L, t)$ decays exponentially with t. As discussed in Sec. III B, the one- and two-state fits are both used to extract $\tilde{\Phi}^{\pm 0}(z, b_\perp, P^z, L)$. As shown in Fig. 12, for the cases with small $\{z, b_\perp\}$ as $\{0a, 1a\}, \{0a, 3a\}, \{2a, 2a\}, \{2a, 3a\}$, the two-state fit results are consistent with one-state ones. However, for the cases with large $\{z, b_\perp\}$, the excited-state contamination cannot be well described with two-state parametrization. Since the excited-state contamination will decrease with the Euclidean time separation increasing, we use the plateau at large t for our one-state fit.

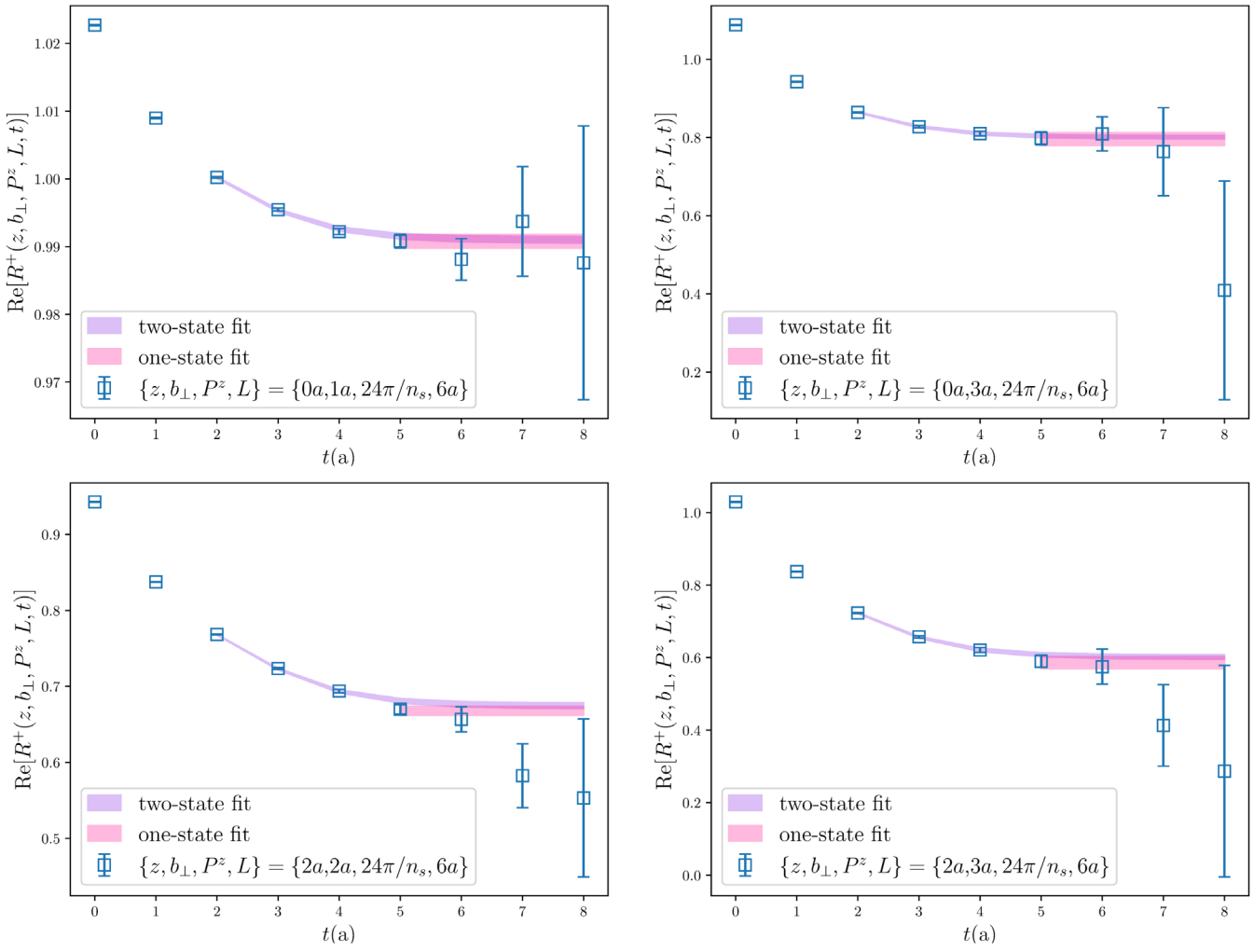

FIG. 12. Four examples for comparing two-state fit and one-state fit to extract the $\tilde{\Phi}^{\pm 0}(z, b_\perp, P^z, L)$ from $R^{\pm}(z, b_\perp, P^z, L, t)$ as described in Sec. III B with $\{z, b_\perp\} = \{0a, 1a\}, \{0a, 3a\}, \{2a, 2a\}, \{2a, 3a\}$, and $\{P^z, L\} = \{24\pi/n_s, 6a\}$. The fit range for two-state fit is $t \in [2a, 8a]$, which for one-state fit is $t \in [5a, 8a]$.

APPENDIX B: GAUGE-LINK LENGTH L DEPENDENCE OF QUASI-TMDWFs

In Sec. III C, the Wilson loop is used to renormalize quasi-TMDWFs, which removes the linear divergence. Similar to the discussion in Sec. III C, we give results with the different $\{P^z, b_\perp, z\}$ in Fig. 13 to show separately the Wilson-link length L

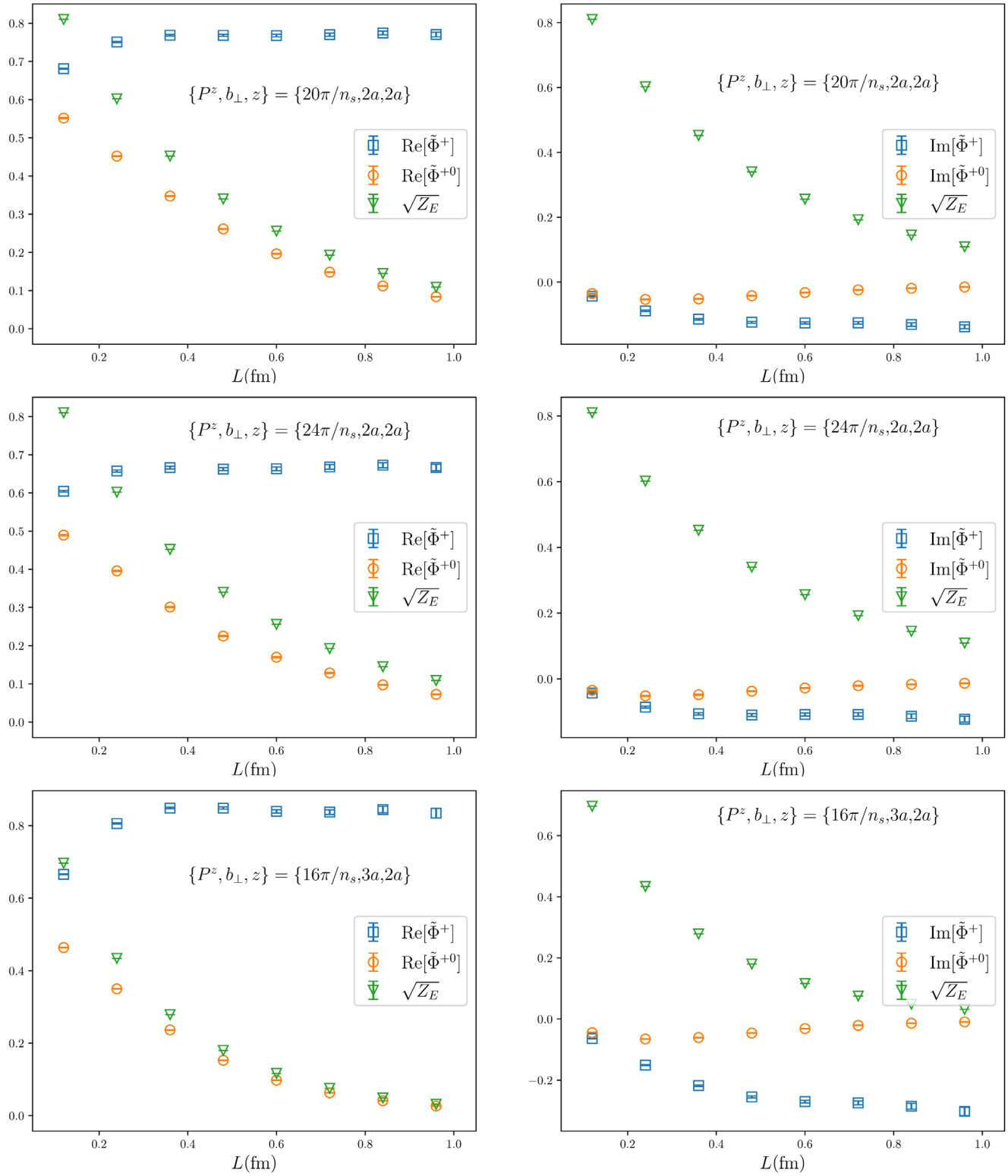

FIG. 13. Results showing the dependence on the gauge line length L of unsubtracted and subtracted quasi-TMDWFs, as well as the Wilson loop with $\{P^z, b_\perp, z\}$ shown in each figure. These results are for $\Gamma = \gamma^z\gamma_5$.

dependence of the Wilson loop, unsubtracted quasi-TMDWFs, and subtracted quasi-TMDWFs. At large L, $\tilde{\Phi}^{+0}$ decays at the same speed of $\sqrt{Z_E}$, so Wilson loop cancels the linear divergence in unsubtracted quasi-TMDWFs.

APPENDIX C: POWER CORRECTION EFFECTS BETWEEN MATCHING

In Sec. III C, we show the comparison of λ dependence of quasi-TMDWFs with $\gamma^t\gamma_5$ and $\gamma^z\gamma_5$. For more cases, we

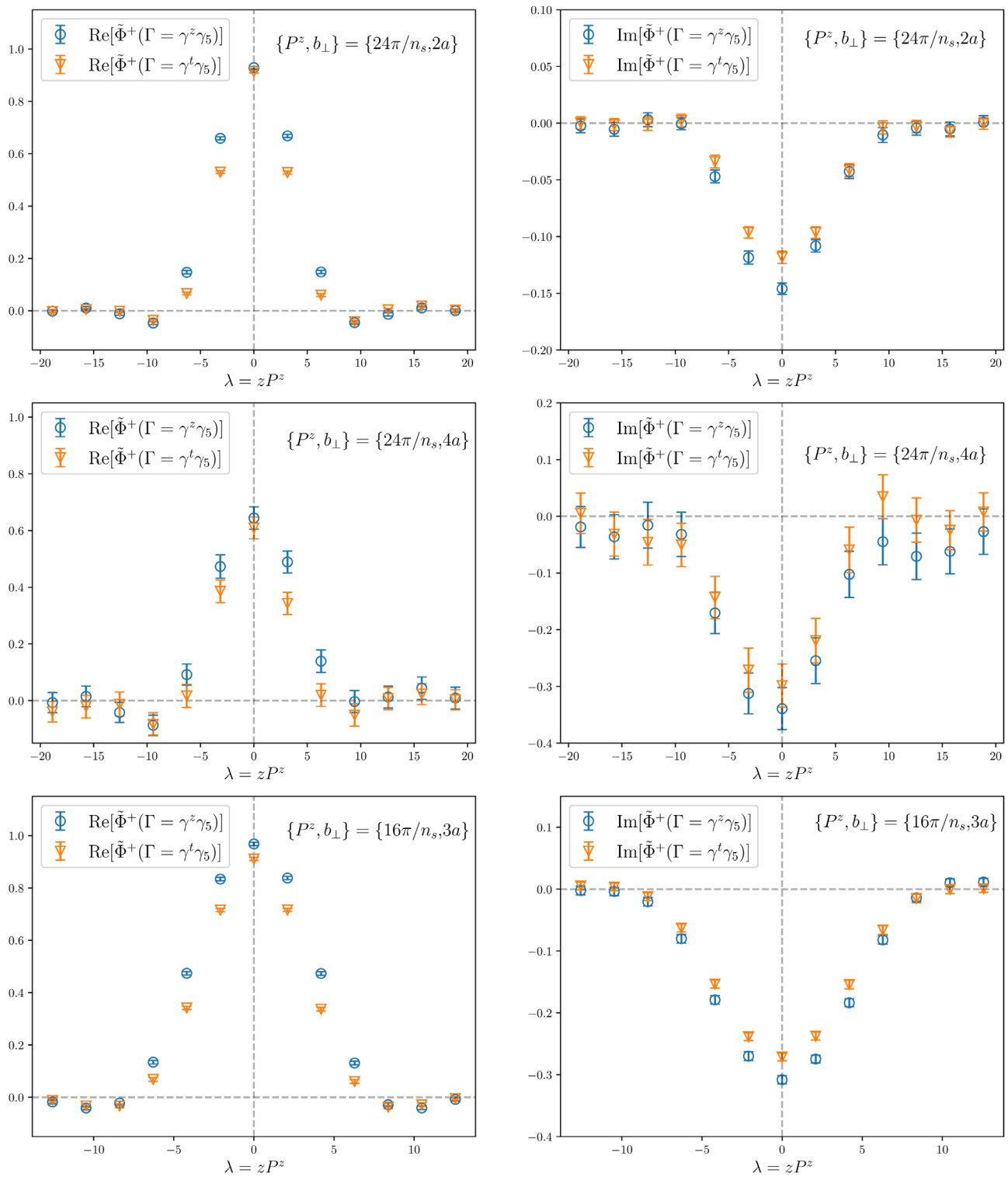

FIG. 14. Examples of comparisons for λ dependence of quasi-TMDWF matrix elements with two Dirac matrices: $\Gamma = \gamma^t\gamma_5$ and $\Gamma = \gamma^z\gamma_5$, with $\{P^z, b_\perp\}$ shown in each figure. Power corrections cause the deviation between both cases.

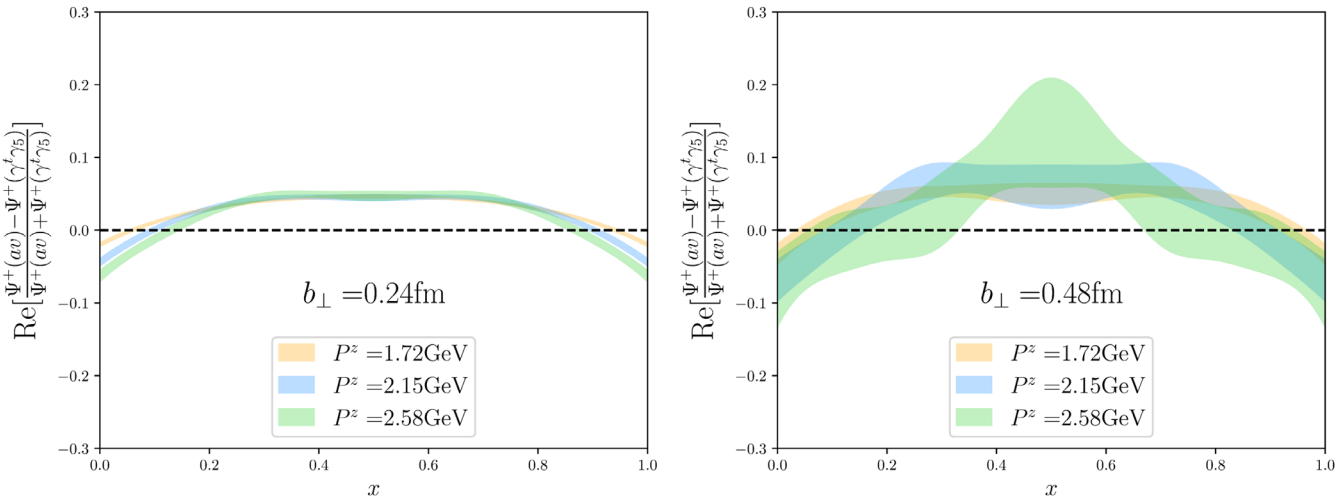

FIG. 15. Comparison of weight factors with $P^z = \{1.72, 2.15, 2.58\}$ GeV at $b_\perp = 0.24$ and 0.48 fm. The P^z independence indicates the higher power corrections have been canceled.

give results with $\{P^z, b_\perp\} = \{24\pi/n_s, 2a\}$, $\{24\pi/n_s, 4a\}$, and $\{16\pi/n_s, 3a\}$ in Fig. 14. Based on these figures, we anticipate that the average of $\gamma^t\gamma_5$ and $\gamma^z\gamma_5$ has reduced the higher power corrections. In order to determine this, we make a comparison of the averaged results and the result with $\Gamma = \gamma^t\gamma_5$. To be explicit, we adopt a normalized difference,

$$A = \frac{\Psi^+(av) - \Psi^+(\gamma^t\gamma_5)}{\Psi^+(av) + \Psi^+(\gamma^t\gamma_5)}, \tag{C1}$$

to reflect the difference between these choices and accordingly the magnitude of high power contaminations. As shown in Fig. 15, this ratio barely depends on P^z for various $b_\perp$ and deviates from zero by about 5%–10%. This indicates the following: (1) Higher-twist effects caused by higher powers of $1/P^z$ are not significant. (2) There are additional momentum-independent corrections. (3) For a large transverse separation b_T, the results also deviate from zero but uncertainties are large. We also rely on our experience with other power corrections. Currently, we think that understanding the origin/behavior of these power corrections requests a detailed exploration on a finer lattice, which we plan to do in the near future.

APPENDIX D: SOME DISCUSSIONS OF THE BRUTE-FORCE FOURIER TRANSFORMATION

In our analysis, we adopt the brute-force Fourier transformation to obtain the quasi-TMDWFs in momentum space. In order to figure out whether the finite separation and truncation will introduce some bias, we do the following analysis.

First, in order to explicitly demonstrate the impact from the tail at large z, we compare different z truncations of Fourier transformation in Fig. 16. One can see that the truncations at $z_{\max} = \{0.72, 0.96, 1.44\}$ fm will lead to overall consistent results. But when one focuses on the extracted CS kernel, like Fig. 17, one notices that the oscillations depend on the chosen truncation. More interestingly, such effects are momentum dependent. The CS kernel is defined as a combination of quasi-TMDWFs with different momentum, and the momentum dependence of truncation effects are also shown in Fig. 17. In these plots, one can see that a stronger truncation of z leads to a stronger oscillation. To deal with the inverse problem, an analyticity-inspired extrapolation in the large-z region was proposed in Ref. [49] and realized in the analysis of LCDAs for a vector meson from lattice QCD [57]. In this project, we did not apply this strategy to the CS kernel, but instead have included these effects as systematic uncertainties.

Second, we made a further exploration on the discreteness of data. Using the available data, we first made an extrapolation and then performed the Fourier transformation. The corresponding results are shown in Fig. 18, with a comparison with a direct Fourier transformation. As shown in this figure, the differences between the two treatments are insignificant. This indicates that the discreteness of data does not induce sizable effects for the oscillation.

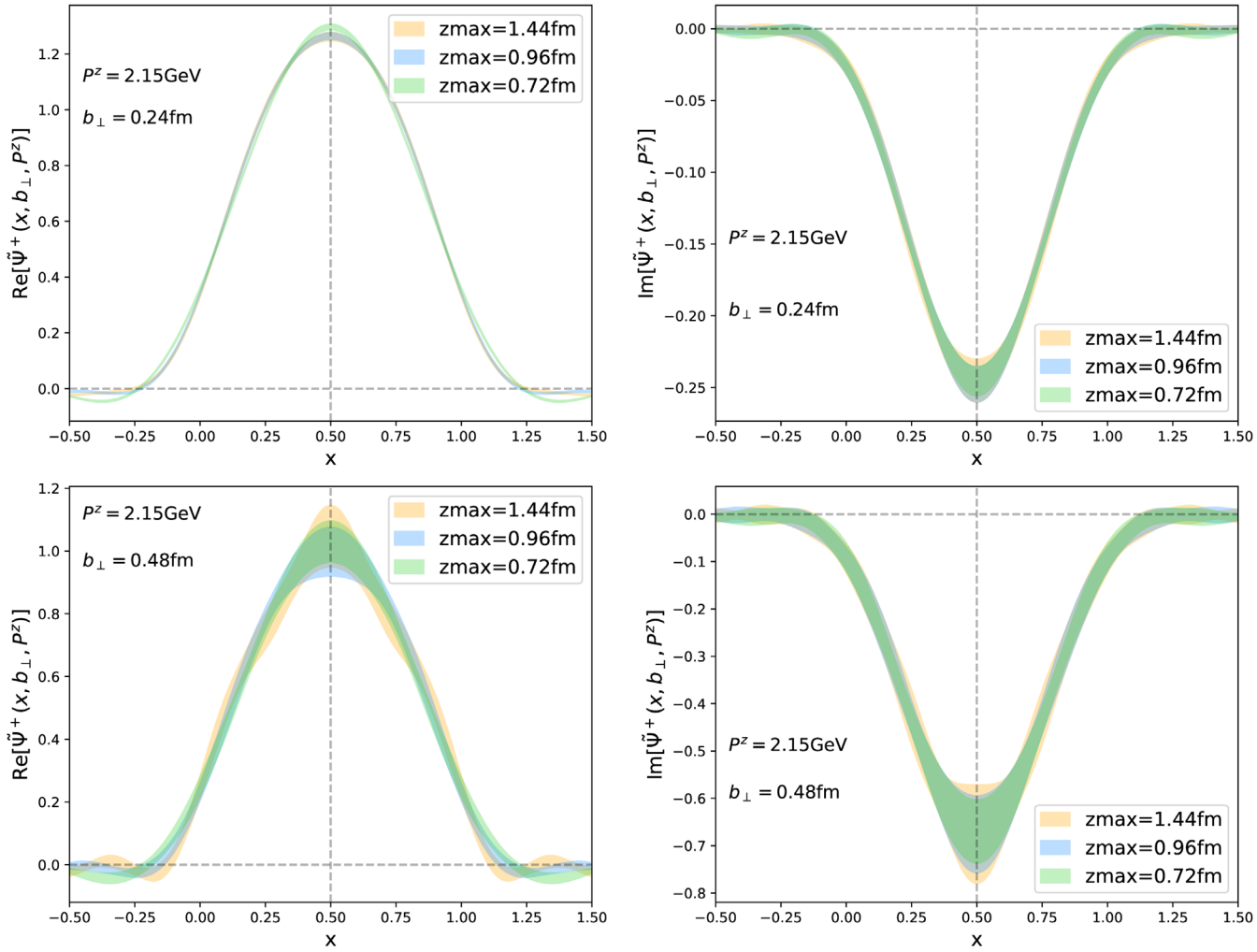

FIG. 16. Quasi-TMDWFs after Fourier transformation with different $z_{\max}$. When $z_{\max}$ is large enough, the Fourier transformation is no longer dependent on the truncation of z.

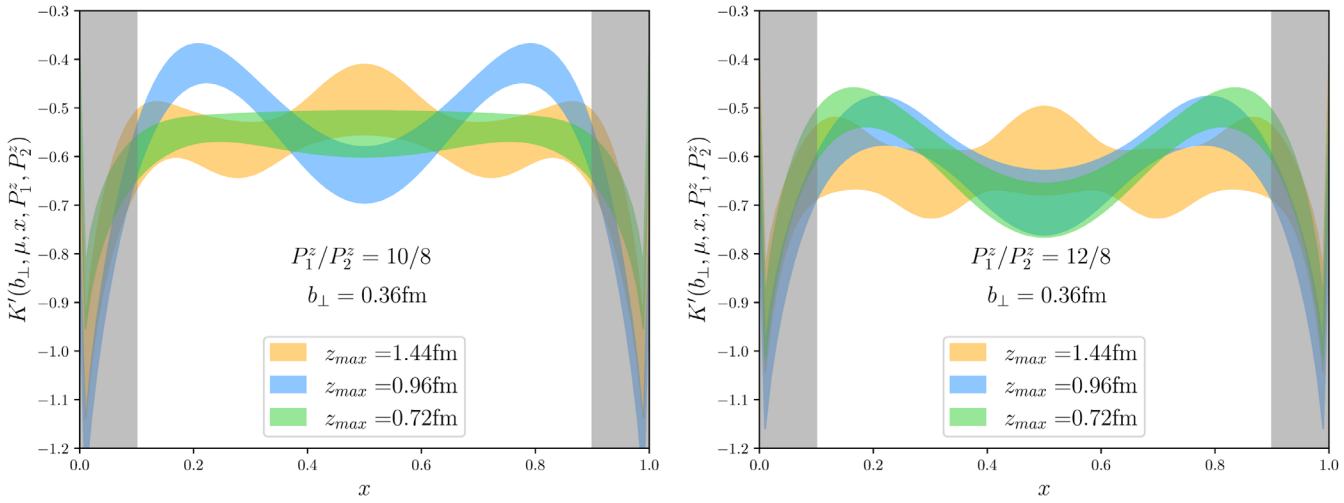

FIG. 17. Comparison of the CS kernel extracted from the quasi-TMDWFs with different truncation at $z_{\max} = \{0.72, 0.96, 1.44\}$ fm. Left: the ones extracted by $\{P_1^z, P_2^z\} = \{2.15, 1.72\}$. Right: the ones extracted with $\{P_1^z, P_2^z\} = \{2.58, 1.72\}$ GeV.

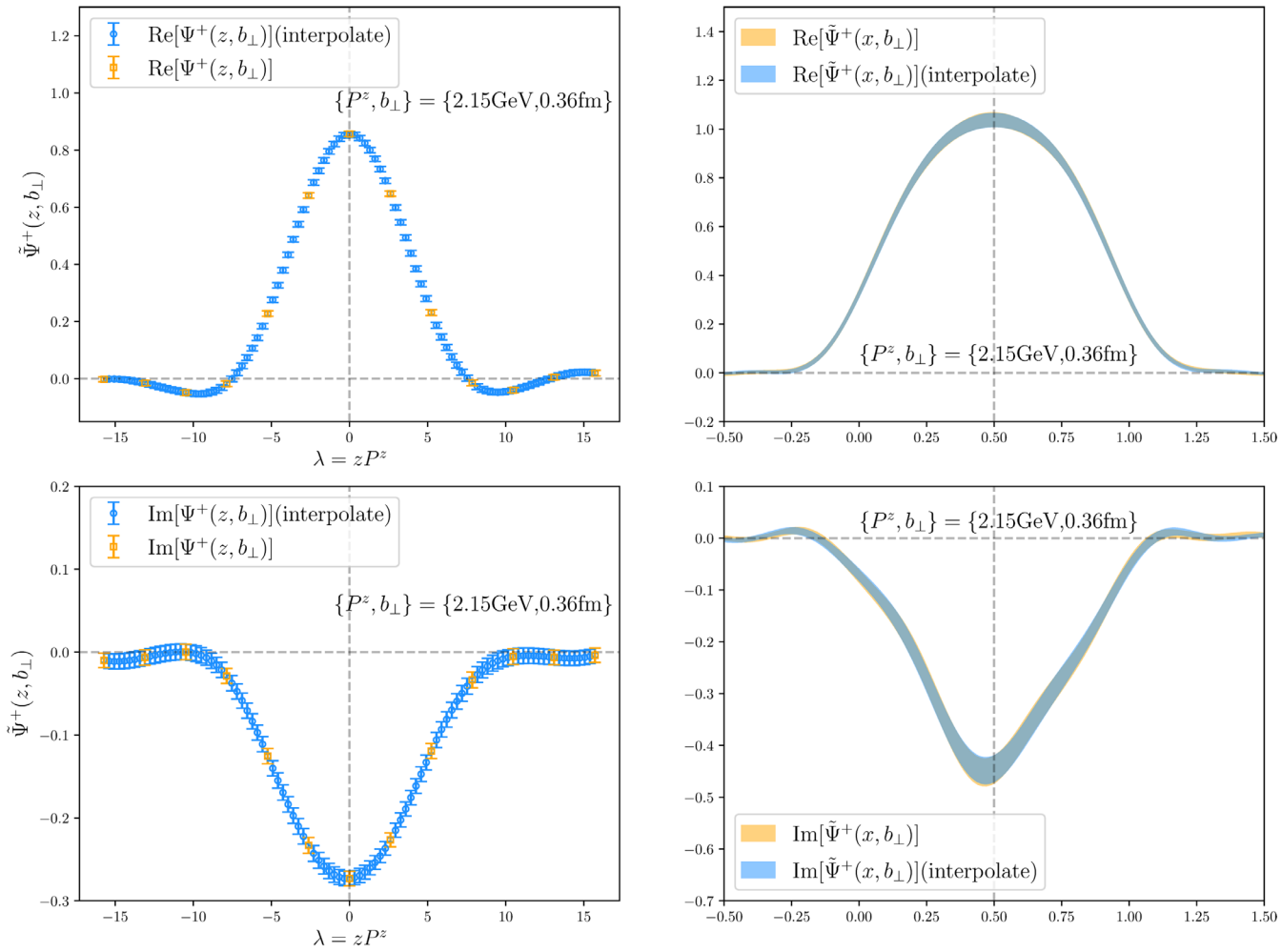

FIG. 18. Comparison of results with and without interpolation.

APPENDIX E: JOINT-FIT DETERMINATION OF COLLINS-SOPER KERNEL

It has been indicated in the main text that different fit ranges as well as parametrization formulas might introduce some arbitrariness into the joint fit. The end-point range can be roughly estimated by the largest attainable λ as $\sim 1/\lambda_{\max}$. For all

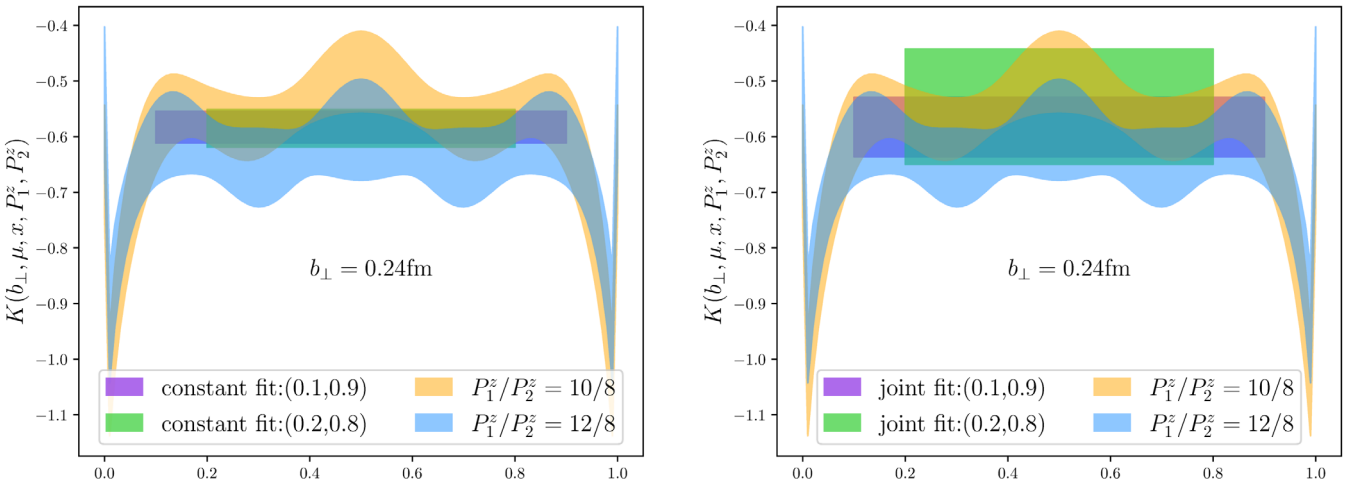

FIG. 19. Comparison of the jointly fitted results for the constant fit and the parametrization in Eq. (30), as well as the fit range with (0.1, 0.9) and (0.2, 0.8). All the fitted bands are consistent with each other.

three momentum cases from 1.72 to 2.58 GeV, the $\lambda_{\max} > 10$, so we estimated the end-point region as [0.1,0.9]. The fitting range dependence indicates our incapability to describe the power corrections. Within the fitting range, the plateau indicates that the influence from power corrections is highly suppressed, so the fit result of parameter A in Eq. (30) is close to 0. Figure 19 shows the comparison of the jointly fitted results for the constant fit (naively setting A to be zero) and the parametrization in Eq. (30), as well as the fit range with (0.1, 0.9) and (0.2, 0.8). We can see that all these fit results are consistent with each other.

[1] John C. Collins and Davison E. Soper, Back-to-back jets in QCD, Nucl. Phys. **B193**, 381 (1981); **B213**, 545(E) (1983).

[2] John C. Collins and Davison E. Soper, Back-to-back jets: Fourier transform from B to K-transverse, Nucl. Phys. **B197**, 446 (1982).

[3] R. Angeles-Martinez *et al.*, Transverse momentum dependent (TMD) parton distribution functions: Status and prospects, Acta Phys. Pol. B **46**, 2501 (2015).

[4] Jozef Dudek *et al.*, Physics opportunities with the 12 GeV upgrade at Jefferson Lab, Eur. Phys. J. A **48**, 187 (2012).

[5] A. Accardi *et al.*, Electron ion collider: The next QCD frontier: Understanding the glue that binds us all, Eur. Phys. J. A **52**, 268 (2016).

[6] R. Abdul Khalek *et al.*, Science requirements and detector concepts for the electron-ion collider: EIC yellow report, 2021.

[7] Daniele P. Anderle *et al.*, Electron-ion collider in China, Front. Phys. (Beijing) **16**, 64701 (2021).

[8] Y. Y. Keum, Hsiang-Nan Li, and A. I. Sanda, Penguin enhancement and $B \to K\pi$ decays in perturbative QCD, Phys. Rev. D **63**, 054008 (2001).

[9] Cai-Dian Lu, Kazumasa Ukai, and Mao-Zhi Yang, Branching ratio and CP violation of $\vec{B}\pi\pi$ decays in perturbative QCD approach, Phys. Rev. D **63**, 074009 (2001).

[10] Makiko Nagashima and Hsiang-nan Li, K_T factorization of exclusive processes, Phys. Rev. D **67**, 034001 (2003).

[11] A. Cerri *et al.*, Report from working group 4: Opportunities in flavour physics at the HL-LHC and HE-LHC, CERN Yellow Rep. Monogr. **7**, 867 (2019).

[12] F. Landry, R. Brock, G. Ladinsky, and C. P. Yuan, New fits for the nonperturbative parameters in the CSS resummation formalism, Phys. Rev. D **63**, 013004 (2000).

[13] F. Landry, R. Brock, Pavel M. Nadolsky, and C. P. Yuan, Tevatron run-1 Z boson data and Collins-Soper-Sterman resummation formalism, Phys. Rev. D **67**, 073016 (2003).

[14] Umberto D'Alesio, Miguel G. Echevarria, Stefano Melis, and Ignazio Scimemi, Non-perturbative QCD effects in q_T spectra of Drell-Yan and Z-boson production, J. High Energy Phys. 11 (2014) 098.

[15] Peng Sun, Joshua Isaacson, C. P. Yuan, and Feng Yuan, Nonperturbative functions for SIDIS and Drell-Yan processes, Int. J. Mod. Phys. A **33**, 1841006 (2018).

[16] Anton V. Konychev and Pavel M. Nadolsky, Universality of the Collins-Soper-Sterman nonperturbative function in gauge boson production, Phys. Lett. B **633**, 710 (2006).

[17] Alessandro Bacchetta, Filippo Delcarro, Cristian Pisano, Marco Radici, and Andrea Signori, Extraction of partonic transverse momentum distributions from semi-inclusive deep-inelastic scattering, Drell-Yan and Z-boson production, J. High Energy Phys. 06 (2017) 081; 06 (2019) 051(E).

[18] Ignazio Scimemi and Alexey Vladimirov, Analysis of vector boson production within TMD factorization, Eur. Phys. J. C **78**, 89 (2018).

[19] Ignazio Scimemi and Alexey Vladimirov, Non-perturbative structure of semi-inclusive deep-inelastic and Drell-Yan scattering at small transverse momentum, J. High Energy Phys. 06 (2020) 137.

[20] Alessandro Bacchetta, Valerio Bertone, Chiara Bissolotti, Giuseppe Bozzi, Filippo Delcarro, Fulvio Piacenza, and Marco Radici, Transverse-momentum-dependent parton distributions up to N^3LL from Drell-Yan data, J. High Energy Phys. 07 (2020) 117.

[21] Xiangdong Ji, Parton Physics on a Euclidean Lattice, Phys. Rev. Lett. **110**, 262002 (2013).

[22] Xiangdong Ji, Parton physics from large-momentum effective field theory, Sci. China Phys. Mech. Astron. **57**, 1407 (2014).

[23] Krzysztof Cichy and Martha Constantinou, A guide to light-cone PDFs from lattice QCD: An overview of approaches, techniques and results, Adv. High Energy Phys. **2019**, 3036904 (2019).

[24] Xiangdong Ji, Yu-Sheng Liu, Yizhuang Liu, Jian-Hui Zhang, and Yong Zhao, Large-momentum effective theory, Rev. Mod. Phys. **93**, 035005 (2021).

[25] Markus A. Ebert, Iain W. Stewart, and Yong Zhao, Towards quasi-transverse momentum dependent PDFs computable on the lattice, J. High Energy Phys. 09 (2019) 037.

[26] Xiangdong Ji, Yizhuang Liu, and Yu-Sheng Liu, TMD soft function from large-momentum effective theory, Nucl. Phys. **B955**, 115054 (2020).

[27] Xiangdong Ji, Yizhuang Liu, and Yu-Sheng Liu, Transverse-momentum-dependent parton distribution functions from large-momentum effective theory, Phys. Lett. B **811**, 135946 (2020).

[28] Xiangdong Ji and Yizhuang Liu, Computing light-front wave functions without light-front quantization: A large-momentum effective theory approach, Phys. Rev. D **105**, 076014 (2022).

[29] Xiangdong Ji, Peng Sun, Xiaonu Xiong, and Feng Yuan, Soft factor subtraction and transverse momentum dependent parton distributions on the lattice, Phys. Rev. D **91**, 074009 (2015).

[30] Phiala Shanahan, Michael Wagman, and Yong Zhao, Collins-Soper kernel for TMD evolution from lattice QCD, Phys. Rev. D **102**, 014511 (2020).

[31] Qi-An Zhang *et al.*, Lattice QCD Calculations of Transverse-Momentum-Dependent Soft Function through Large-Momentum Effective Theory, Phys. Rev. Lett. **125**, 192001 (2020).
[32] Maximilian Schlemmer, Alexey Vladimirov, Christian Zimmermann, Michael Engelhardt, and Andreas Schäfer, Determination of the Collins-Soper kernel from lattice QCD, J. High Energy Phys. 08 (2021) 004.
[33] Yuan Li *et al.*, Lattice QCD Study of Transverse-Momentum Dependent Soft Function, Phys. Rev. Lett. **128**, 062002 (2022).
[34] Phiala Shanahan, Michael Wagman, and Yong Zhao, Lattice QCD calculation of the Collins-Soper kernel from quasi-TMDPDFs, Phys. Rev. D **104**, 114502 (2021).
[35] Markus A. Ebert, Iain W. Stewart, and Yong Zhao, Determining the nonperturbative Collins-Soper kernel from lattice QCD, Phys. Rev. D **99**, 034505 (2019).
[36] Thomas Becher and Matthias Neubert, Drell-Yan production at small q_T, transverse parton distributions and the collinear anomaly, Eur. Phys. J. C **71**, 1665 (2011).
[37] Jui-yu Chiu, Ambar Jain, Duff Neill, and Ira Z. Rothstein, The Rapidity Renormalization Group, Phys. Rev. Lett. **108**, 151601 (2012).
[38] Ye Li and Hua Xing Zhu, Bootstrapping Rapidity Anomalous Dimensions for Transverse-Momentum Resummation, Phys. Rev. Lett. **118**, 022004 (2017).
[39] S. Moch, B. Ruijl, T. Ueda, J. A. M. Vermaseren, and A. Vogt, Four-loop non-singlet splitting functions in the planar limit and beyond, J. High Energy Phys. 10 (2017) 041.
[40] Yao Ji, Jian-Hui Zhang, Shuai Zhao, and Ruilin Zhu, Renormalization and mixing of staple-shaped Wilson line operators on the lattice revisited, Phys. Rev. D **104**, 094510 (2021).
[41] Markus A. Ebert, Stella T. Schindler, Iain W. Stewart, and Yong Zhao, Factorization connecting continuum & lattice TMDs, J. High Energy Phys. 04 (2022) 178.
[42] E. Follana, Q. Mason, C. Davies, K. Hornbostel, G. P. Lepage, J. Shigemitsu, H. Trottier, and K. Wong, Highly improved staggered quarks on the lattice, with applications to charm physics, Phys. Rev. D **75**, 054502 (2007).
[43] K. Symanzik, Continuum limit and improved action in lattice theories. 1. Principles and ϕ^4 theory, Nucl. Phys. **B226**, 187 (1983).
[44] A. Bazavov *et al.*, Lattice QCD ensembles with four flavors of highly improved staggered quarks, Phys. Rev. D **87**, 054505 (2013).
[45] Anna Hasenfratz and Francesco Knechtli, Flavor symmetry and the static potential with hypercubic blocking, Phys. Rev. D **64**, 034504 (2001).
[46] Xiangdong Ji, Jian-Hui Zhang, and Yong Zhao, Renormalization in Large Momentum Effective Theory of Parton Physics, Phys. Rev. Lett. **120**, 112001 (2018).
[47] Tomomi Ishikawa, Yan-Qing Ma, Jian-Wei Qiu, and Shinsuke Yoshida, Renormalizability of quasiparton distribution functions, Phys. Rev. D **96**, 094019 (2017).
[48] Jeremy Green, Karl Jansen, and Fernanda Steffens, Nonperturbative Renormalization of Nonlocal Quark Bilinears for Parton Quasidistribution Functions on the Lattice Using an Auxiliary Field, Phys. Rev. Lett. **121**, 022004 (2018).
[49] Xiangdong Ji, Yizhuang Liu, Andreas Schäfer, Wei Wang, Yi-Bo Yang, Jian-Hui Zhang, and Yong Zhao, A hybrid renormalization scheme for quasi light-front correlations in large-momentum effective theory, Nucl. Phys. **B964**, 115311 (2021).
[50] Xiang-Dong Ji and M. J. Musolf, Subleading logarithmic mass dependence in heavy meson form-factors, Phys. Lett. B **257**, 409 (1991).
[51] Yi-Kai Huo *et al.*, Self-renormalization of quasi-light-front correlators on the lattice, Nucl. Phys. **B969**, 115443 (2021).
[52] G. Peter Lepage and Paul B. Mackenzie, On the viability of lattice perturbation theory, Phys. Rev. D **48**, 2250 (1993).
[53] Jiunn-Wei Chen, Xiangdong Ji, and Jian-Hui Zhang, Improved quasi parton distribution through Wilson line renormalization, Nucl. Phys. **B915**, 1 (2017).
[54] Jian-Hui Zhang, Jiunn-Wei Chen, Xiangdong Ji, Luchang Jin, and Huey-Wen Lin, Pion distribution amplitude from lattice QCD, Phys. Rev. D **95**, 094514 (2017).
[55] Bernhard U. Musch, Philipp Hagler, John W. Negele, and Andreas Schafer, Exploring quark transverse momentum distributions with lattice QCD, Phys. Rev. D **83**, 094507 (2011).
[56] Jian-Hui Zhang, Luchang Jin, Huey-Wen Lin, Andreas Schäfer, Peng Sun, Yi-Bo Yang, Rui Zhang, Yong Zhao, and Jiunn-Wei Chen, Kaon distribution amplitude from lattice QCD and the flavor SU(3) symmetry, Nucl. Phys. **B939**, 429 (2019).
[57] Jun Hua, Min-Huan Chu, Peng Sun, Wei Wang, Ji Xu, Yi-Bo Yang, Jian-Hui Zhang, and Qi-An Zhang, Distribution Amplitudes of K^* and ϕ at the Physical Pion Mass from Lattice QCD, Phys. Rev. Lett. **127**, 062002 (2021).